Controls of mantle plumes and lithospheric folding on modes of intraplate continental tectonics: differences and similarities

Evgueni Burov[1] and Sierd Cloetingh[2]

[1]*ISTEP UMR CNRS* 7193*, Université Pierre et Marie Curie,* 4 *Place Jussieu,* 75252 *Paris Cedex* 05*, France. E-mail: evgenii.burov@upmc.fr*
[2]*Netherlands Research Centre for Integrated Solid Earth Sciences, VU University Amsterdam, Faculty of Earth and Life Sciences, De Boelelaan* 1085*,* 1081 *HV Amsterdam, The Netherlands*

SUMMARY
Mantle plume activity and lithospheric folding by far-field stresses exerted from plate boundaries are two important end-members as mechanisms for continental intraplate deformation. The topographic expression of mantle plume impingement on continental lithosphere and lithospheric folding has some striking similarities. Observations from a number of areas in Europe's intraplate lithosphere demonstrate that these mechanisms commonly interact in space and time. We present the results of thermomechanical modelling addressing the role of factors such as the presence of a hot upper mantle, the spatial dimensions of the plume and the time constants involved in the temporal succession of plume activity and lithospheric folding by stress accumulation in intraplate continental lithosphere. The results demonstrate that both the processes, plume–lithosphere interactions and folding may interact resulting either in strong amplification, attenuation or modification of their surface expression. These inferences are compatible with a number of key observations on the nature and the temporal succession of topography evolution in the Alpine foreland, the Pannonian Basin, the Scandinavian continental margin and the Iberian Peninsula.

Key words: Creep and deformation; Intra-plate processes; Continental margins: convergent; Continental margins: divergent; Dynamics of lithosphere and mantle; Dynamics: convection currents, and mantle plumes; Hotspots.

GJI Tectonics and geodynamics

1 INTRODUCTION

Over the last few years a series of mechanisms have been proposed for the creation of anomalous continental topography in plate interiors (Schubert *et al.* 2001; Cloetingh *et al.* 2005; Allen & Davies 2007). These include mantle-convection with time-dependent upper mantle flow and the potential effects of the rheological stratification of the lithosphere (Schmeling & Marquart 1990, 1993), megaplumes, commonly considered as a cause for large-scale continent-wide tilting and vertical motions (Mitrovica *et al.* 1989; Lithgow-Bertelloni & Gurnis 1997; van Keken 1997; Jellinek *et al.* 2003) and magmatic underplating often advocated as a cause for large-scale uplift and volcanism in rifted margin settings (Clift 1999; Skogseid *et al.* 2000). Many observations exist, however, for regional-scale intraplate deformation of periodic and punctuated nature, frequently linked in time and space to plate-tectonic reorganizations in oceanic spreading patterns, continental breakup and temporal changes in plate convergence rates and directions (Ziegler *et al.* 1998).

At regional scale, folding and plume–lithospheric interactions (PLIs, Fig. 1) appear to be both important mechanisms for periodic intraplate deformation operating on timescales of 1–20 Ma. Although both have received much attention in the last few years (e.g. Burov & Guillou-Frottier 2005; Burov *et al.* 2007; Cloetingh & TOPO-EUROPE Team 2007), many controversial interpretations

remain (Foulger *et al.* 2000; Lustrino & Carminati 2007), both in terms of modelling concepts and observations. As was pointed out by Burov *et al.* (2005, 2007), PLI in continental domains may result in periodical surface undulations with several characteristic wavelengths: 50–100 km, 150–200–300 km and 400–500 km. These wavelengths are much smaller than those commonly inferred for PLI (∼1000 km). The wavelength reduction or modulation, and its multiharmonic character result from a pronounced rheological stratification of the continental lithosphere that serves both as a damper, which reduces plume impact due the presence of a viscous crustal channel, and as a wavelength converter for the plume 'signal' (Fig. 1a). Upon its emplacement, the plume head exerts flexural deformation in the overlying plate, as well as basal shear and traction, which result in development of mechanical instabilities. Such instabilities systematically develop in stratified media with strong rheological contrasts (strong upper crust–weak ductile upper crust–strong intermediate crust–weak ductile intermediate crust–strong lower crust–weak ductile lower crust–strong mantle lithosphere, etc.). The characteristic wavelengths of this deformation are proportional to 4–10 thicknesses of the respective competent layers in the crust and mantle, and have little to do with the wavelength of the applied load (plume). Weak ductile channels formed by the lower or intermediate crust in thermally young lithospheres (<300–500 Ma old) may be quite thick (10–20 km), with viscosities as
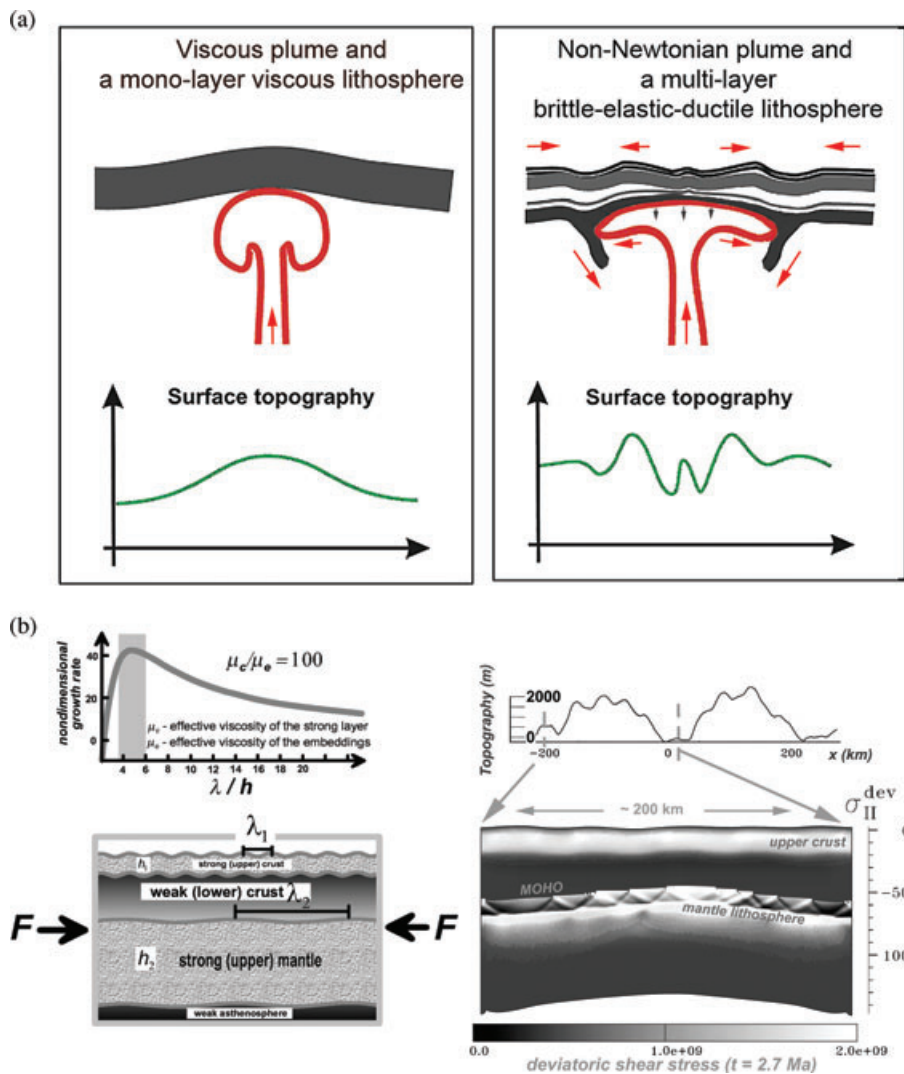
Figure 1. (a) Sketch of plume–lithosphere interaction. The conventional models (left-hand panel) predict only long-wavelength (controlled by the plume head size) isostatic topography due to plume impact. Accounting for plate rheology and multilayer lithosphere structure (right-hand panel) yields a more complex response, with several short-wavelengths generated by intraplate deformation, tectonic-style deformation at surface and strong lithosphere mantle erosion at depth. In that case, the short wavelengths are controlled by the thickness of the lithosphere and intralithospheric layers, not by the plume head size. (b) Llithospheric folding. Left-hand panel: Sketch showing that the multilayer structure of the lithosphere (causing crust–mantle decoupling) may result in several wavelengths of folding controlled by thicknesses of the lithosphere as a whole and of various intralithospheric layers: mantle lithosphere, upper or intermediate crust and so on. Interaction between the stiff layers may also produce some intermediate wavelengths. Right-hand panel: Example of previous numerical experiments on 'decoupled' folding from Cloetingh *et al.* (1999) that demonstrate that superposition of mantle (long-wavelength) and crustal (shorter wavelength) folding may yield two different characteristic wavelengths at surface.

low as 10^{20}–10^{21} Pa s (e.g. Avouac & Burov 1996). Such channels may mechanically fully or partly decouple mantle and crustal deformation; specifically it may damp vertical undulations (<2 km) of the mantle layer caused by a plume. The predicted surface wavelengths fall in the range that is more commonly referred to tectonic-scale deformation, in particular continental lithosphere folding (e.g. Burov *et al.* 1993; Cloetingh *et al.* 1999). Damping will not occur only in cases without mechanical stratification [old continental plates (>500 Ma), strong lower crustal composition (e.g. dry diabase, oceanic plates]. These circumstances have been discussed in Guillou-Frottier *et al.* (2007) who have pointed out that folding and plumes can yield similar surface expressions for most continental plates (Fig. 1a). In fact, geological evidence exists in a number of areas for a succession in time of plume activity and folding (e.g. Cloetingh *et al.* 1999). The conventional definition for plumes deals

with a localized Rayleigh–Benard instability originating from the lower mantle, more or less constantly fed by the material coming from great depths to the surface. It should be noted that the plume size has a strong influence on the weakening of the overlying continental lithosphere (Burov & Guillou-Frottier 2005). Many researchers have drawn attention to the association of plume activity and magmatic activity (e.g. Wilson & Patterson 2001).

In this paper, we investigate a number of scenarios with the aim to quantify the possible interaction in space and time between both mechanisms (Fig. 1a). To that aim we explore end-member cases of folding and plume activity as well as scenarios where plume activity is followed by folding and vice versa. In this context, we quantify strain and stress patterns characteristic for intraplate deformation as well as other diagnostics characterizing the surface expression. We compare the model inferences with observations for

a number of areas (Fig. 2a) where evidence exists for plume-folding interaction including the Alpine foreland, the Pannonian basin, the Scandinavian continental margin and the Iberian Peninsula.

Over the last few years, the results from seismic tomography have been crucial in arguments pro and contra the presence of plumes (see Barth *et al.* 2007, for a review). This applies in particular to the depth extent of the inferred upper mantle low-velocity anomalies and their connection with the lower mantle (e.g. Bijwaard & Spakman 1999; Goes *et al.* 1999; Foulger *et al.* 2000; Thybo & Anderson 2006). At the same time there appears to be growing consensus on the occurrence of strong lateral heterogeneity in the upper mantle underlying for example the European continental lithosphere
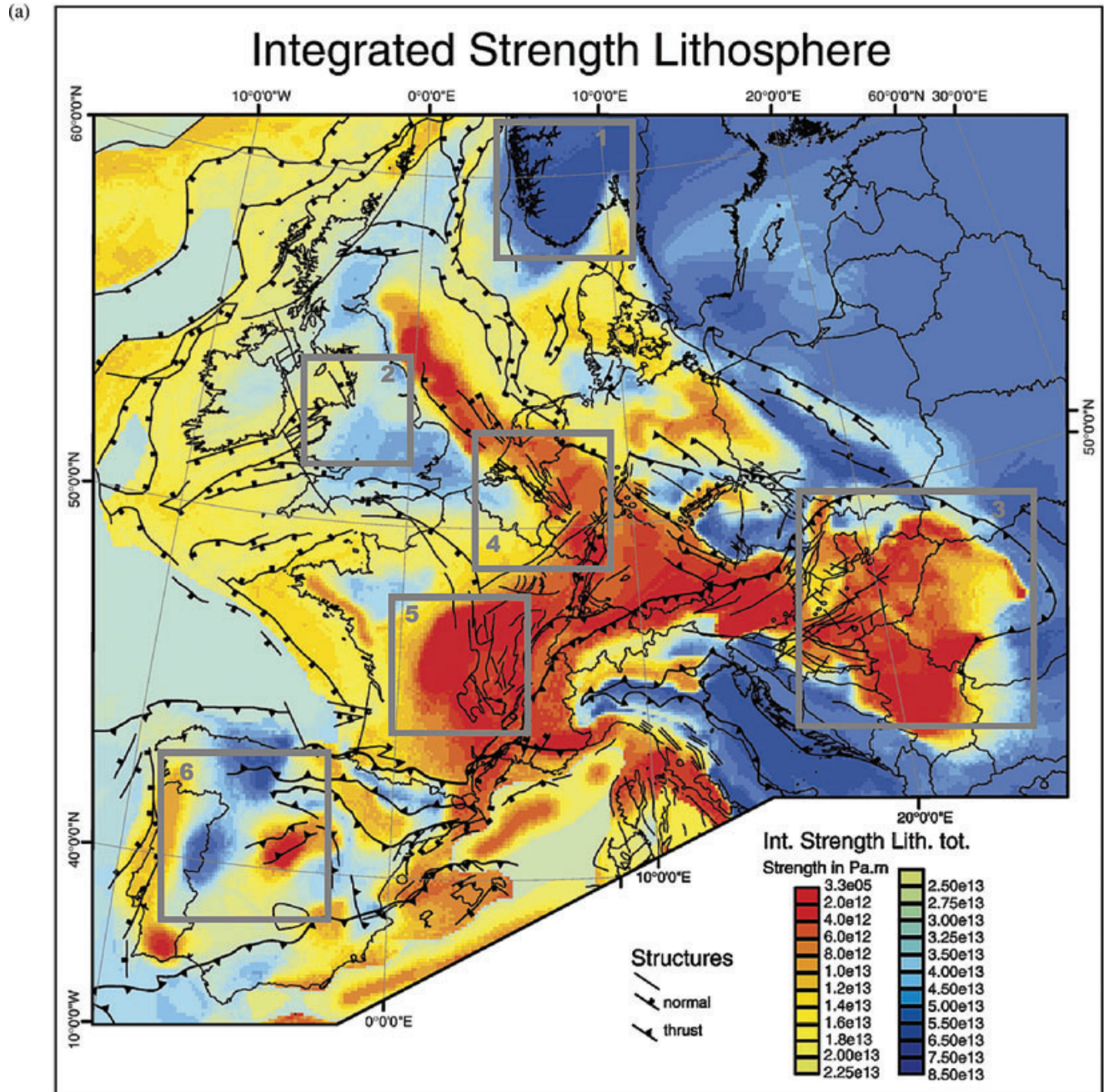

Figure 2. (a) Distribution of present-day integrated lithospheric strength of Europe (after Cloetingh *et al.* 2005; Tesauro *et al.* 2007) with areas affected by plume and folding activity: (1) Norway (Rohrmann *et al.* 2002; Smelror *et al.* 2007); (2) British Isles (Arrowsmith *et al.* 2005); (3) Pannonian basin (Cloetingh *et al.* 1999; Gemmer & Houseman 2007); (4) Eifel (Ritter *et al.* 2001); (5) Massif Central (Granet *et al.* 1995); (6) Iberia (Cloetingh *et al.* 2002; de Vicente *et al.* 2007); Morocco (Babault *et al.* 2008; Ghorbal *et al.* 2008; not shown on the map). High-strength areas in the lithosphere basically generate larger wavelengths of deformation than weaker areas. (b) Tomographic cross-sections through some areas of intraplate Europe displaying evidences for upper mantle perturbations. Top panel: Results of local tomography imaging of a 'baby' plume under the Eifel area (Ritter *et al.* 2001). Middle panel: regional tomographic cross-section corrected for crustal thickness variations (Tesauro *et al.* 2008) through the Massif Central area (Koulakov *et al.* 2009) with low-velocity upper mantle anomaly below the Massif interpreted by Granet *et al.* (1995) as baby plume. Bottom panel: Regional tomographic cross-section through the Pannonian basin showing a wide anomalous upper mantle area with low seismic velocities (Wortel & Spakman 2000).
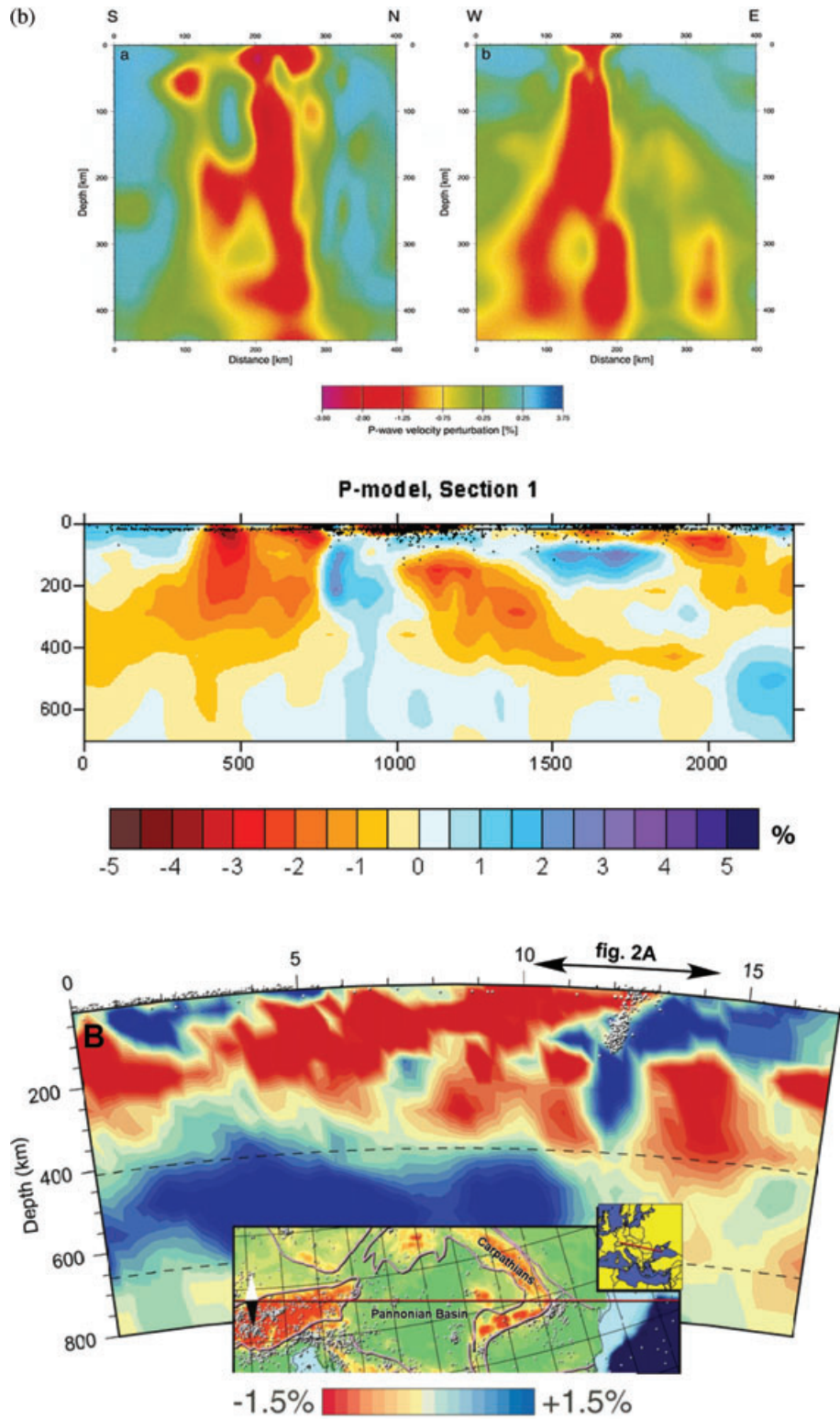
Figure 2. (*Continued.*)

(e.g. Goes *et al.* 2000; Wortel & Spakman 2000; Ritter *et al.* 2001; Piromallo & Morelli 2003; Koulakov *et al.* 2009, see Fig. 2b).

The presence of relatively hot upper mantle has been inferred for a number of areas making part of the European Cenozoic rift system (Dèzes *et al.* 2004), basins created by Neogene backarc extension in the Alpine/Mediterranean area such as the Tyrrhenian Sea and the Pannonian Basin, but also for realms of the Northern Atlantic, including the Southern part of Scandinavia and the British Isles (Arrowsmith *et al.* 2005). Another striking feature affecting the connection between deep Earth processes and surface topography in continental Europe (Cloetingh & TOPO-EUROPE team 2007) appears to be the presence of baby plumes imaged by local

tomography studies in the Eifel area of Germany (Ritter *et al.* 2001, Fig. 2b) and the French Massif Central (Granet *et al.* 1995; Koulakov *et al.* 2009, see also Fig. 2b). As has been shown by quantitative modelling of the thermomechanical structure of the European lithosphere (Cloetingh *et al.* 2005; Tesauro *et al.* 2007), the presence of a relatively hot upper mantle under large areas in Western and Central Europe has led to the presence of a relatively weak lithosphere, which renders this area prone to present-day deformation under the influence of stress fields generated at Europe's plate boundaries. This is in marked contrast with the inferred presence of strong lithosphere in the Eastern European Platform, underlain by a thick lithosphere and a cold upper mantle. The differences between the two segments of Europe's intraplate lithosphere located west and east of the Tornquist-Teisseyre line is also manifested in the spatial distribution of seismicity and inferences on rigidity inferred from gravity studies (Pérez-Gussinyé & Watts 2005), residual mantle gravity anomalies (Tesauro *et al.* 2007) and *Vp/Vs* ratios (Artemieva *et al.* 2006).

Simultaneously with the accumulating evidence for a thermally perturbed upper mantle under Western and Central Europe, a large data base has been build up on the intraplate stress field distribution affecting Europe's lithosphere from focal mechanism studies, borehole break-outs and neotectonic field studies (World Stress Map 2007). These studies have demonstrated a close link between stresses in the plate interior and plate boundary forces exerted at the plate margins. These findings are corroborated by results from numerical studies (e.g. Golke & Coblentz 1996; Jarosiński *et al.* 2007) highlighting also second order contributions to the stress field distribution from spatial variations in plate rigidity, thermal perturbations in the upper mantle and body forces induced by topographic anomalies (e.g. Bada *et al.* 1998).

It appears that areas such as the Nortwestern European foreland, the Pannonian basin, the continental margins of the Northern Atlantic and Central and Western Iberia are presently under the influence of intraplate compression, largely as a result of Africa/Europe convergence and Atlantic ridge push. With a lithosphere characterized by relatively low strength due to a weak mantle lithosphere as inferred for the Pannonian Basin and most of the European Cenozoic Rift System, stresses appear to be close to limits required to lead to lithospheric failure by compressionally induced folding of the lithosphere.

A number of numerical (e.g. Burov *et al.* 1993; Burov & Molnar 1998; Cloetingh *et al.* 1999, 2002) and analogue tectonic experiments (e.g. Sokoutis *et al.* 2005; Dombrádi *et al.* 2008; Fernández-Lozano *et al.* 2008) as well as an extensive set of observational studies (e.g. LeFort & Agarwal 1996; Bourgeois *et al.* 2007; Ziegler & Dèzes 2007) have provided support for this mechanism as a prime control on neotectonics of Central Asia, the NW European foreland, the Pannonian Basin and Iberia.

In a recent study (Burov *et al.* 2007; Guillou-Frottier *et al.* 2007), we have drawn attention to some striking similarities in the topographic expression for these two end-member processes in continental intraplate deformation. Below we will examine their interplay through a set of numerical modelling experiments carried out in detailed comparison with a large body of geological and geophysical constraints.

Key questions addressed will be the relative effectiveness of amplification by folding of plume-induced lithosphere deformation and topography and vice versa and the response times and time-lags involved. Another question is whether 'baby' plumes are more efficient in localizing deformation than large plumes. A typical feature of plume-affected folding appears to be acceleration of surface uplift (folding goes into saturation when plastic hinges form at the inflexion points of the folds). As will be demonstrated, for the discrimination of plumes and folding it is key to access constraints on presence or absence of radial versus linear symmetry, heat flow anomalies, gravity and geoid data. Important in this respect is, for example, the role of hot lithosphere in localizing deformation in passive rifted continental passive margins (Scheck-Wenderoth & Maystrenko 2008) and backarc basins (Horváth & Cloetingh 1996; Cloetingh *et al.* 2006). Another factor examined is the effect of differences in convergence rates. In this context, it should be noted that areas such as the Pannonian Basin (Grenerczy *et al.* 2005, see also Cloetingh *et al.* 2007), the Northwestern European foreland (Dèzes *et al.* 2004; Tesauro *et al.* 2005), Iberia (Cloetingh *et al.* 2002; Fernández-Lozano *et al.* 2008) and Morocco (Babault *et al.* 2008) are located at different distances from the Africa–Europe Plate boundary. The areas examined allow an examination of the effect of differences in thermomechanical age of the lithosphere and their consequences for the onset of the deformation and the wavelength of the induced topography. The models and their comparison with data also enable a quantification of the deformation versus time.

2 OBSERVATIONS

Inspection of the topographic/GTOPO30 map of an area spanning from the Northern Atlantic to Northern Africa and from the North/Central Atlantic to the East European platform demonstrates the existence of major differential intraplate topography, closely associated with ongoing vertical motions. A comparison with the spatial distribution of present-day lithospheric strength (Cloetingh *et al.* 2005; Tesauro *et al.* 2007, Fig. 2a) suggests that the intraplate seismicity of Europe appears to be primarily localized along pre-existing weakness zones such as the European Cenozoic Rift System, marked by thinned crust (Tesauro *et al.* 2008) or areas with anomalous topography such as Southern Norway (Rohrmann *et al.* 2002).

The spatial variations in lithospheric strength and crustal thickness are constrained by a dense coverage by geophysical observations. At the same time, for many of the areas where present-day intraplate deformation occurs, seismological and geochemical evidence exists for a relatively hot upper mantle (e.g. Hoernle *et al.* 1995; Goes *et al.* 2000; Pilidou *et al.* 2005) and/or thinned lithosphere (Cloetingh *et al.* 2006).

As pointed out above, the record of intraplate deformation of the lithosphere of Europe and surrounding areas allows to examine a spectrum of plume and folding interactions. For example, the southern Norwegian continental rifted margin appears to have been affected by a large deep-seated plume emplaced during continental break-up (Skogseid *et al.* 2000) followed by several phases of compressional deformation (Doré *et al.* 2000; Lundin & Dore 2002). Seismic tomography (Arrowsmith *et al.* 2005) has demonstrated the occurrence of relatively hot upper mantle under the British Isles in conjunction with areas of low gravity, overprinted by present-day compression (Bott & Bott 2004). The Pannonian Basin of Central Europe was affected by plume activity and the emplacement of a hot astenosphere followed by late stage compressional reactivation within 20 Myr after backarc extension (Horvath *et al.* 2006).

The Alpine foreland of northwestern Europe, in particular the Eifel area and the French Massif Central also experienced an interplay of Neogene emplacement of baby plumes (Granet *et al.* 1995; Ritter *et al.* 2001) and lithospheric folding (Bourgeois *et al.* 2007; Ziegler & Dèzes 2007).

The Iberian microplate (Cloetingh *et al.* 2002; De Vicente *et al.* 2007) and the adjacent areas of the Gulf of Cadiz (Zittelini *et al.* 2009) and the Atlas mountains of Morocco (Missenard *et al.* 2006) have experienced lithospheric folding and a variable degree of asthenospheric upwelling during Cenozoic convergence of Africa and Europe in the near field of the collision zone (De Vicente *et al.* 2008). Constraints on the timing and prime features of intraplate deformation in these areas and a summary of data on thermomechanical ages of the lithosphere at the onset of plume activity are provided in Table 1.

A comparison with cratonic cases is not straightforward as their areal extent is limited in Western and Central Europe, apart from craton-like cases such as the Paris Basin (Robin *et al.* 2003). We, therefore, refer for a comparison to cratonic Australia, Africa, Northern America, Siberia, the Russian craton and the Scandinavian shield. Of these, one of the most prominent cases of intraplate deformation is presented by the Central Australian craton (Stephenson & Lambeck 1985). For end-member plume cases we refer to Northern and Eastern Africa (e.g. Burov *et al.* 2007; Guillou-Froittier *et al.* 2007).

It should be noted that widespread evidence exists for previously inverted basins locked in folding (see Cloetingh & van Wees 2005), such as for example the Ferghana basin in Central Asia (thermo-mechanical age 150 Ma, convergence rate: 2.5 cm yr^{-1}; Burov & Molnar 1998) and the Pannonian Basin: 30 Ma (Alpine thickening event, Oligocene thickening).

3 PLUME–LITHOSPHERE INTERACTIONS AND FOLDING OF CONTINENTAL LITHOSPHERE: PHYSICAL FRAMEWORK

3.1 Plume–lithosphere interactions

The physical aspect of the mantle plume concept includes upwelling of low density, high temperature and low viscosity mantle material separated from large-scale convective motions (e.g. Sleep 2006). This upwelling, if continuously fed from a deeper source area, can form a «superplume», that is, a persisting diapir of very large scale coming from the D″ boundary (e.g. Condie *et al.* 2000; Romanowicz & Gung 2002). There may be also smaller scale diapirs originating from different depths (Courtillot *et al.* 2003; Montelli *et al.* 2004; Ritter 2005). In many situations, a Newtonean plume tail may stay connected to its 'mushroom' head for quite a long time after the plume head emplacement, but for more appropriate non-Newtonean rheologies (e.g. Davies 1994; Trompert & Hansen 1998) the plume can also ascend in chaotic or pulsating regimes characterized by high ascent rates, which may result in loss of the plume tail, and, hence, in interruption of its material supply from the source region. The resulting thermomechanical consequences for surface geodynamics and geology appear to be largely dependent on the chosen model (structural, thermal and mechanical regimes) of the lithosphere (Burov & Guillou-Frottier 2005; Burov *et al.* 2007).

We assume that the plume ascent in a depth interval *d–h* is driven by a density contrast $\Delta\rho$, which maximal value (at the bottom) is $\Delta\rho_{max}$:

$$\Delta\rho_{max} = (\rho_p \alpha \Delta T_{max} + \Delta\rho_{ch}), \quad (1)$$

where *d* is the depth to the bottom of the mantle, *h* is the depth to the bottom of the lithosphere, ρ_p is the density of plume material at embedding temperature at depth *d* and ΔT_{max} is the difference between temperatures of plume material and surrounding mantle

Table 1. Temporal and spatial characteristics of some folding and plume events affecting European and North African continental lithosphere.

Area	Timing of the plume (Myr)	Onset of folding (Myr)	Lag (Myr)	Initial thermo mechanical age of the lithosphere, (Myr)	Wave-length (km)	Amount of shortening	Rate (mm yr^{-1})	Crustal thickness (km)	Reference
Pannonian Basin	15	5–0	10–15	30/18–5	50 crust 250 mantle		4	28	Cloetingh *et al.* (2006), Horvath *et al.* (2006)
Eifel	1–0	17–0	–17–16	20–200/37–17	270			35	Bourgeois *et al.* (2007)
Norwegian margin	35	45–15 ?– 0	–10–0	200/250–65/250–65	20 crust	3 per cent		15–35	Vagnes *et al.* (1998), Doré *et al.* (2000), Skogseid *et al.* (2000)
Iberia	10	–0	10–50	120–350/170–130	50 crust 200 mantle		4–5	35	Cloetingh *et al.* (2002), De Vicente *et al.* (2007, 2008)
Morocco	10	33 13	–23 –3	100/170–130	200	10 per cent		35 (Atlas) 30 (Meseta)	Ghorbal *et al.* (2008), Babault *et al.* (2008)
Massif Central	–0	17–0		20–200/37–17	270			25	Ritter (2005), Wyns *et al.* (2003), Bourgeois *et al.* (2007)
British Isles	60			80				35	Arrowsmith *et al.* (2005)

at depth h, and $\Delta\rho_{ch}$ is the chemical density contrast (we assume a median value of 10 kg m^{-3} (e.g. Schubert *et al.* 2001). $\Delta\rho$ is not constant because the plume cools down when it ascends, and because the temperature of the surrounding mantle increases with depth. Rapidly ascending plumes (high Péclet numbers) will not strongly cool conductively, and, even if one takes into account the effect of decompression cooling (Herzberg 1995), the temperature contrast between the plume and the ambient mantle upon its arrival at the bottom of continental lithosphere rather increases than decreases.

Even for such a small and by present time thermally relaxed plume such as Massif Central plume, Sobolev & Babeyko (1994) and Sobolev *et al.* (1997) find a temperature plume anomaly below the lithosphere with average potential temperature of 1700 °C or, more importantly, '200–250 °C higher than the average temperature of the upper mantle'. The maximal thermal anomaly should be higher than 200–250 °C since seismic data provide averaged estimates. Since this plume event is not that recent, the temperature of the flattened plume head upon its emplacement could be couple of hundred degrees higher than its actual temperature.

Hence, taking also into account the increase of the coefficient of thermal dilatation with decreasing depth (e.g. Schubert *et al.* 2001), the plume density contrast and thus driving buoyancy force basically grow with decreasing depth resulting in acceleration of the plume ascent rate at shallow depths. Under adiabatic conditions, the viscosity of the subasthenosphere mantle increases with depth due to the growing pressure and changes in the mineralogical composition. This also contributes to the increase of the plume ascent rate with decreasing depth.

In non-Newtonian fluids, a very small variation in buoyancy forces results in a strong variation in the plume (diapir) ascent behaviour and in the way the plume head spreads below the lithosphere (e.g. Weinberg & Podladchikov 1994; d'Acremont *et al.* 2003; Burov & Guillou-Frottier 2005). For equivalent body forces, this ascent may be orders of magnitude faster than that for a Newtonian fluid. It is noteworthy that non-Newtonian behaviour is restricted to 'cold' deformation characterized by high effective viscosities and deviatoric stresses in excess of several MPa. Such stresses can be produced only in the mantle above and near the bottom of the lithosphere. Hence, non-Newtonian behaviour controls only the final emplacement of the plume head and the lithosphere. The deeper mantle is likely to be controlled by low-stress Newtonian diffusion creep, which linearly depends on the differential stress. For this reason we use a constant minimal viscosity cut-off in the model (see Section 4.4).

Schmeling & Marquart (1990, 1993) have previously shown that the effect of loading a continental lithosphere from below (plume head impingement) on topography may be strongly influenced by the rheological stratification. These authors have found and quantified this effect, as well as the time-dependence of topography due to time-dependent upper mantle flow. However, the effect of stratified viscoelastoplastic properties and free surface was not yet treated in numerical models of PLI. Till now, the consequences of plume head-continental lithosphere (PH-CL) interactions are mainly derived from conventional models of viscous mantle convection (e.g. Farnetani & Richards 1994; Sleep 1997, 2003a,b,c, 2006; Cserepes *et al.* 2000). In terms of lithospheric response, the predictive power of these fluid dynamics models is limited because they do not adequately account for a stratified viscoelastoplastic lithosphere. In common convection models (e.g. Doin *et al.* 1997), the lithosphere is considered as a thin viscous or quasi-viscous layer with an undeformable surface. Although this assumption is acceptable

for oceanic plates, the continental lithosphere cannot be regarded as a thin layer because its thickness (150–300 km) constitutes 50–90 per cent of the thickness of the convective part of the upper mantle (350–500 km). In contrast with oceanic lithosphere, continental lithosphere is highly stratified as it is composed of a 30–70 km thick highly buoyant crust, which is quartz-rich, and a 60–250 km thick negatively or neutrally buoyant mantle layer of basic composition (olivine). The crust also counts several layers including brittle-elastic upper crust, brittle–ductile elastic middle and elastic-ductile lower crust. Due to the presence of quartz-rich aggregates, the lower crust may have a viscosity (e.g. Kirby & Kronenberg 1987) as low as $10^{20}–10^{21}$ Pa s below 15–20 km depth (250–400 °C). Consequently, the high viscosity (mainly brittle) upper crust is mechanically decoupled from the strong olivine-rich lithospheric mantle, in which ductile creep is activated at high temperature (750–800 °C).

As a consequence of the crust-mantle decoupling, mantle deformation due to plume head impingement may produce only a moderate or strongly modulated impact on surface deformation. According to recent studies, the presence of a thick stratified viscoelastoplastic continental lithosphere may substantially alter the surface expression of PLIs (Burov & Guillou-Frottier 2005; Burov *et al.* 2007; Guillou-Frottier *et al.* 2007, Fig. 1a). Indeed, conventional monolayer models of PLI predict long-wavelength deformation with dynamic surface topography of 1–1.5 km (e.g. Ribe & Christensen 1994). This prediction stems from the assumption that vertical undulations of the lithosphere–mantle boundary are directly translated to the surface. This assumption is highly questionable for continents because 1.5 km vertical displacements of the mantle–lithosphere boundary can be accommodated within a 15–30 km thick ductile lower crustal layer while the other (viscoelastic or viscoelastoplastic) layers can relax plume-related stresses over significant periods of time (up to 10 Myr). Basically, with this rheological layering, the surface topography will not simply replicate the topography of the mantle–lithosphere boundary. In addition, mechanical decoupling between the crust and mantle and the dependence of bending stresses on yield stress and plate curvature result in lateral variations of integrated plate strength and tension–compression instabilities that may yield short-wavelength topography (Burov & Diament 1995; Burov & Guillou-Frottier 2005).

3.2 Large-scale folding

Folding is a characteristic unstable deformation that may develop in stratified media with significant competence contrasts, such as the lithosphere, in response to horizontal loading (Biot 1961; Ramberg 1961). These instabilities may develop under compression or basal shear as a result of strain–stress incompatibility on the interfaces of the mechanical layers of different strength. At the initial stages of deformation, compression instabilities lead to appearance of periodic folds with an exponential growth rate and a dominating wavelength, λ, roughly proportional to 5–10 times the thickness(es) of the competent core(s) within the lithosphere, h ($h = 10–100$ km, i.e. $\lambda = 50–1000$ km).

'Biot's,' or linear, folding encompasses the cases where compression of the lithosphere takes place from the beginning, leading to the formation of alternating basins and highs, and where the conditions of the linear theory are more or less satisfied (thin layer approximation, no strain-softening, plain layers, etc.). In the case of linear folding in a Newtonian medium, an asymptotic relation derived from the thin layer equilibrium equation is quite simple

(Biot 1961; Ramberg 1961):

$$\lambda_1 = 2\pi h(\mu_{l1}/6\mu_{l2})^{1/3}. \tag{2}$$

Here λ_1 is the 'Laplacian' dominant wavelength of folding in the absence of gravity, h is the thickness of the competent layer (crustal or mantle), and μ_{l1} and μ_{l2} are the effective viscosities (or competencies) of the strong layer and weak surrounds, respectively. The above equation, derived assuming no gravity, provides estimates of $\lambda_1/h = 20$–40 for typical competence contrasts. This does not hold for most lithospheric-scale cases, where $\lambda/h = 4$–6 is more common due to the influence of the gravity-dependent terms. A reduction of the normalized characteristic wavelength to values around 4 is also predicted for power law or plastic layers (e.g. Smith 1979). In the simplest case of a single stiff viscous layer on top of an inviscid medium, the dominant gravity-dependent harmonics can be accounted as (e.g. Burov & Molnar 1998) :

$$\lambda_g \sim 2\pi[2h\dot{\varepsilon}\,\mu_{\rm eff}/(\Delta\rho g)]^{1/2}, \tag{3}$$

where $\Delta\rho$ is the density contrast, $\dot{\varepsilon}$ is the strain rate, $\mu_{\rm eff}$ is the effective ductile viscosity (see Appendix A), n is the power-law exponent and h is the thickness of the competent layer.

At large amounts of shortening this deformation may become aperiodic (e.g. Hunt *et al.* 1996) so that the wavelength and amplitude of folding start to vary along the deformed transect. The mentioned plume-induced periodical deformations actually also refer to folding or boudinage caused by basal shear at the bottom of the lithosphere. However, the other major cause for folding of continental lithosphere is tectonic loading by horizontal far-field forces. For characteristic parameters of various layers within the continental lithosphere ($h = 10$–120 km, $\mu = 10^{19}$–10^{26} Pa s; $\Delta\rho = 10$–600 kg m^{-3}), eq. (2) and (3) predict folding wavelengths that may vary from as low as 30 km (upper crustal folding) to as high as 600–800 km. These wavelengths fall in the range of the lithospheric wavelengths that can be generated by PLIs (Burov & Guillou-Frottier 2005) suggesting all possible interferences between folding and PLI. It is noteworthy that these interferences do not require compatibility of folding and plume related strain rates in the lithosphere.

3.3 Plume-folding interferences

Taking into account the possibly periodical character of instable topographic response to plume impingement, it appears that this response may effectively interfere with the periodic instable response of the lithosphere in case of its large-scale folding provoked by horizontal tectonic loading (e.g. Burov *et al.* 1993; Cloetingh *et al.* 1999; Gerbault *et al.* 1999). Since the folding and PLI should produce similar wavelengths of deformation, it is likely that interaction between the two processes may result both in strong amplification or attenuation of the deformation, depending on the eventual phase shift between the wavelengths produced by folding and PLI.

4 MODEL AND EXPERIMENTS

4.1 Model setup

We exploit the earlier results obtained in the parametric studies by Burov & Guillou-Frottier (2005), Burov *et al.* (2007) and d'Acremont *et al.* (2003) who have modelled plume–continental lithosphere interactions for various viscoelastoplastic lithospheric structures, plume head sizes and Rayleigh numbers. We also use

the results from our earlier studies on lithospheric folding (Burov *et al.* 1993; Cloetingh *et al.* 1999; Gerbault *et al.* 1999). We apply the same approach based on the numerical code derived from FLAC algorithm (Cundall 1989; Poliakov *et al.* 1993). This method handles realistic viscoelastoplastic rheologies and upper surface boundary conditions. To account for pressure-dependent deformation (Mohr–Coulomb plasticity, ductile creep at great depth) and free upper surface, this method solves Newtonian equations of motion (second law) instead of Navier–Stokes flow equations commonly used in plume-convection models. The algorithm explicitly takes into account elastic brittle–ductile properties of the mantle, crust and lithosphere, and handles brittle and ductile strain localization, which permits to model formation of brittle and ductile faults and shear zones. The free upper surface boundary condition allows for an adequate account of the deformation of the lithosphere. Due to the explicit nature of this elastically compressible code, the temperature, gravity and pressure-dependent body forces are computed directly without the necessity to use assumptions such as potential temperature. The recent versions of the code were described in full detail elsewhere (Burov & Poliakov 2001; Burov *et al.* 2001, 2003; Burov & Guillou-Frottier 2005). Therefore, we restrict the description of the method to a résumé provided in the Appendix A.

4.2 Model geometries

We investigate the development of folding and mantle plume-like instabilities through a model (Fig. 3) that includes lithospheric plates of various thermotectonic ages [60, 150, 300 and 1000 Ma, in terms of half-space cooling model with radiogenic heating developed by Burov & Diament (1995) on the base of the earlier model of Parsons & Sclater (1977)] that experiences horizontal shortening at different rates, from slow to rather fast (1.5, 3 and 6 cm yr^{-1}). Following previous plume models (e.g. Ribe & Christensen 1994), we skip the initial (deep mantle) stages of plume rise, as they are of minor importance for the near-surface evolution. In the experiments, the initial mantle plume is located at the base of the model box, and has a diameter of 100 or 200 km. We chose a spherical shape for the initial plume because translating viscous bodies take a spherical shape in laminar regime at significant distance from the surface (Batchelor 1967). This assumption corresponds to mid-mantle conditions. Nevertheless, since the model plume head is deformable, the choice of its initial geometry is of minor importance. The vertical size of the model is 650 km (upper mantle), its horizontal size is 1800 km (Fig. 3).

In the first set of experiments, the plume rises below the lithosphere in the absence of tectonic compression. In the second set of experiments, the lithosphere undergoes compression without a plume at the base of the model. In the third set of experiments, the plume rises below a simultaneously compressed lithosphere.

4.3 Density and rheological structure

Each element of the numerical grid is assigned its specific material phase defined as a subset of physical parameters of the corresponding material: density, thermal and EVP rheology parameters (Tables 2 and 3). We use a conventional density and rheology structure for the mantle and lithosphere (Turcotte & Schubert 2002; Burov & Watts 2006, Fig. 3). All models include a 40-km-thick crust and four horizontal rheological layers (Tables 2 and 3; Carter &
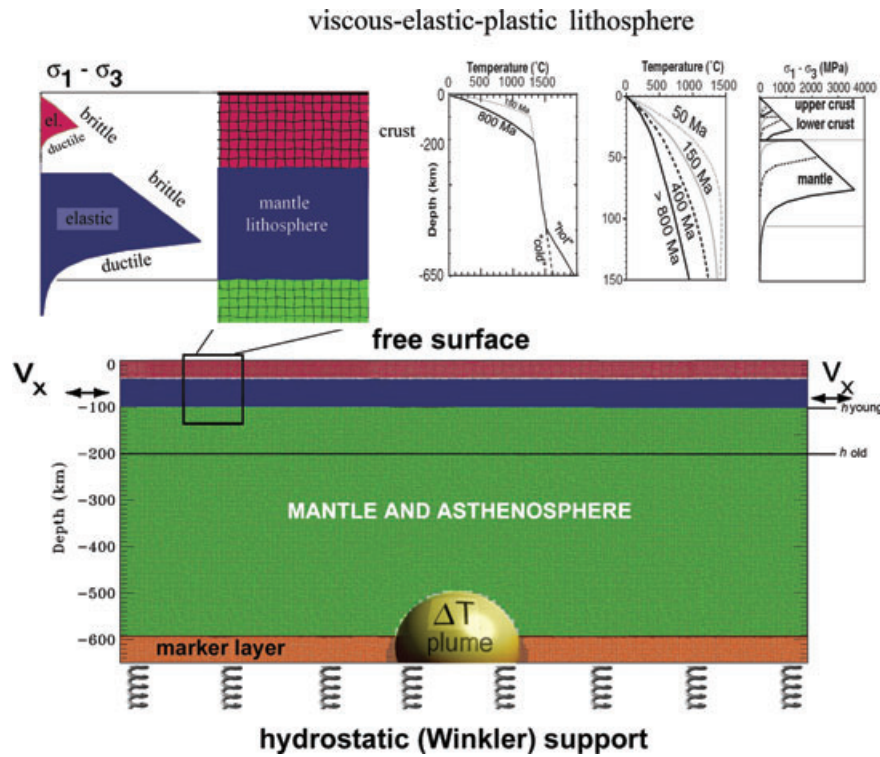
Figure 3. Numerical model setup. A visco-elastic-plastic rheology is used for various structural units of the model [upper crust (quartz-dominated), lower crust (quartz-dominated or diabase rheology), lithosphere mantle (dry olivine), sublithosphere upper mantle(dry olivine)]. The upper surface is free allowing for a self-consistent prediction of lithospheric response to plume impact and far-field compression forces. On the left-hand side, top insert shows a yield-stress envelope (YSE) for continental lithosphere that results from a combination of elastic, plastic and ductile properties (Tables 2 & 3) for a given lithology (quartz-dominated upper and lower crust, olivine dominated mantle). On the right-hand side, top insert shows mantle and lithosphere geotherms and YSEs (diabase lower crust) for different thermotectonic ages and two end-member mantle geotherms : 'cold' (whole mantle convection) and 'hot' (stratified convection, with distinct cells in the upper and lower mantle).

Table 2. Notations and physical values common for all experiments (Schubert *et al.* 2001; Turcotte & Schubert 2002).

Parameter	Values and units	Definition
σ, τ	Pa, MPa	Stress (complete, deviatoric)
P	Pa, MPa	Pressure
u	m, mm	Displacement vector
v	m s^{-1}, mm an^{-1}	Velocity vector
$\dot{\varepsilon}$	s^{-1}	Strain rate
μ	10^{19}–10^{25} Pa s	Effective viscosity ($\tau/\dot{\varepsilon}$)
T	°C, K	Temperature
h_c	40 km	Moho depth
h_l	100–250 km	Thickness of lithosphere
h_m	60–210 km	Thickness of lithosphere mantle
D	100–200 km	Plume diameter
ρ_c	2800 kg m^{-3}	Average density of the crust
ρ_l	3330 kg m^{-3}	Density of mantle lithosphere
ρ_m	3340 kg m^{-3}	Reference deep mantle density
ρ_p	$\rho_m + \Delta\rho_{ch} + \alpha\rho_m\Delta T$	Plume density
$\Delta\rho_{ch}$	0–25 kg m^{-3}	Chemical density contrast
g	9.8 m s^{-2}	Acceleration due to gravity
C_p	10^3 J Kg^{-1} °C^{-1}	Specific heat
ΔT	250 °C	Initial temperature contrast plume – background
α	3×10^{-5} °C^{-1}	Thermal expansion coefficient at 0 km depth
β	8×10^{-12} Pa^{-1}	Isothermal compressibility

Tsenn 1987; Kirby & Kronenberg 1987): (1) a 20-km-thick granitic upper crust with a density of 2700 kg m^{-3}; (2) a 20-km-thick quartz-dominated lower crust with an effective rheology of dry granite and a density of 2900 kg m^{-3}; (3) a 60- or 160-km-thick olivine mantle lithosphere with a density of 3330 kg m^{-3}; and (4) the reference density of mantle at the bottom of the lithosphere is $\rho_m =$ 3340 kg m^{-3} so that the lithosphere is initially gravitationally stable (Turcotte & Schubert 2002). We do not test different reference

Table 3. Specific rheology and related thermal parameters.

Parameter	Value
All rocks	
λ, G Lamé elastic constants ($\lambda = G$)	30 GPa (above 250 km depth)
λ, G Lamé elastic constants ($\lambda = G$)	60 GPa (below 250 km depth)
ϕ friction angle (Mohr–Coulomb criterion)	30°
C_0 cohesion (Mohr–Coulomb criterion)	20 MPa
Specific upper or weak (quartz) lower-crust properties	
ρ (upper crust)	$\rho_{cu} = 2700$ kg m^{-3}
ρ (lower crust)	$\rho_{cl} = 2900$ kg m^{-3}
n	2.4
A	6.7×10^{-6} MPa^{-n} s^{-1}
Q	1.56×10^5 kJ mol^{-1}
Specific strong lower crust properties (diabase or basalt)	
ρ	2980 kg m^{-3}
n	3.4
A	2×10^{-4} MPa^{-n} s^{-1}
Q	2.6×10^5 kJ mol^{-1}
Specific mantle properties (olivine)	
ρ (lithosphere)	$\rho_l = 3330$ kg m^{-3}
n	3
A	1×10^4 MPa^{-n} s^{-1}
Q	5.2×10^5 kJ mol^{-1}
Thermal model	
Surface temperature (0 km depth), T_0	0 °C
Temperature at the bottom of lithosphere, T_m	1330 °C
Temperature at 660 km depth	1700 °C (cold model)
Temperature at 660 km depth	2000 °C (hot model)
Average thermal conductivity, k	3.5 Wm^{-1} °C^{-1}
Thermal conductivity of crust, k_c	2.5 Wm^{-1} °C^{-1}
Thermal conductivity of mantle, k_m	3.5 Wm^{-1} °C^{-1}
Thermal diffusivity of mantle, χ	10^{-6} m^2 s^{-1}
Surface radiogenic heat production, H_s	9.5×10^{-10} W kg^{-1}
Radiogenic heat production decay depth, h_r	10 km
Thermotectonic age of the lithosphere, a	60 (young) to 1000 Ma (old)

Notes: Compilation by Burov *et al.* (2001). ρ is density; Q, n, A are material-dependent parameters of ductile flow laws (Kirby & Kronenberg 1987; Kohlstedt *et al.* 1995). Other parameters from Turcotte & Schubert (2002).

densities for the mantle, because the density of the model plume has the same dependence on pressure and temperature as the background, and hence the absolute values of the background density are not important. The eq. (1) defines the initial density contrast between the plume and the mantle. The thermal part of this contrast varies as the plume cools down due to thermal exchanges with the surrounding mantle and due to the fact that the temperature of the surrounding mantle decreases as the plume progresses to the bottom of the lithosphere. A uniform numerical grid (300×130 elements) provides a vertical and horizontal resolution of 5 km per element (Fig. 3). The lithosphere counts 30–50 elements in vertical cross-section, which provides 10–15 times better resolution than common plume models (e.g. Ribe & Christensen 1994).

4.4 Boundary and initial conditions

4.4.1 Mechanical boundary conditions

The mechanical boundary conditions assigned on the four sides of the box (Fig. 3) are: at the left- and right-hand sides, horizontal velocity, v_x; at the bottom, hydrostatic pressure with free slip in all directions; the upper surface is free (free stress and free slip condition in all directions), with moderate diffusion erosion ($k = 500$ m^2 yr^{-1}). In the experiments on PLIs without folding, the horizontal velocity

at the borders is dynamically adjusted to allow accommodation of the overall extension produced by the plume. For that, the following automatic procedure was applied: we first evaluate stresses arriving from plume head spreading (=plume buoyancy), starting from the moment when the plume head intrudes the mantle lithosphere (this moment is defined automatically when plume-head markers arrive above the bottom of the lithosphere). We then compute the horizontal velocity that has to be applied at the borders of the model to maintain corresponding stress level in the competent layers of the lithosphere. This velocity is applied along the entire lateral sides of the model. For the folding experiments, the horizontal velocity is constant.

4.4.2 Thermorheological initial conditions

Zero outflow is assumed as a lateral thermal condition on both sides of the box. The initial background geotherm is obtained by joining the continental and deep mantle (adiabatic) geotherms. Fixed temperatures are used as upper (0 °C) and lower boundary condition (1700 °C for 'cold' geotherm or 2000 °C for 'hot' geotherm). The initial age-dependent geotherms in the lithosphere are computed according to Parsons & Sclater (1977) and Burov & Diament (1995). Since the thermal structure of lithospheric plates becomes nearly stationary after reaching an age of 400–500 Ma (e.g. Burov &

Diament 1995, 1996), and does not practically change after 700 Ma, the maximal tested age of the lithosphere was 1000 Ma.

The lithospheric geotherm (Fig. 3) becomes adiabatic (~0.3 °C km^{-1}, Sleep 2003c) at depths below an isotherm of 1330 °C; the temperature slowly increases from 1330 to 1400 °C at 400–500 km depth (e.g. Ribe & Christensen 1994) and then to 1700 °C-(whole mantle convection, 'cold geotherm') 2000 °C (layered two level convection, 'hot geotherm') at 650 km depth. The assumption of a rapid temperature rise within the bottom layer is justified if the thermal convection in the upper mantle (Ra > 10^5) is separated from convection in the lower mantle (Ra ~ 10^4, stratified, or layered convection hypothesis). In this case main temperature changes must be concentrated in the upper and bottom thermal boundary layers of the upper mantle. In the upper boundary layer (lithosphere) the temperature rises from 0 to 1330 °C within the interval of the first 150–250 km from the surface (e.g. Jaupart *et al.* 2007). The geothermal gradient becomes small within the nearly isothermal kernel below (70–100 °C change in the depth interval between the bottom of the lithosphere and roughly 500 km depth in case of stratified convection, or 650 km depth in case of whole mantle convection). For stratified convection, Schubert *et al.* (2001) admit the possibility of more than 1000 °C temperature rise at the bottom of the upper mantle, compared to the mid-mantle temperature (in this study we assume a value of 600 °C, which yields 2000 °C at the bottom of the upper mantle). In case of whole mantle convection, the temperature gradient at the bottom of the upper mantle remains adiabatic, yielding roughly a 200–300 °C temperature rise compared to the mid-mantle temperature (1700 °C at the bottom). The available experimental data are uncertain, and hence it is equally possible for the bottom temperatures in the upper mantle to be as low as 1600 °C (whole mantle convection) or as high as 2700 °C (layered convection) (Schubert *et al.* 2001). In this study, we primary assume the double-layer convection ('hot' geotherm, 2000 °C at the base of the upper mantle) but we also test the model sensitivity to the assumption of single-layer convection ('cold' geotherm, 1700 °C at the base of the upper mantle).

The upper part (lithosphere–asthenosphere) of the initial thermal model is validated by computing key stagnant parameters (according to Solomatov 1995; Solomatov & Moresi 2000; Nyblade & Sleep 2003; Sleep 2003c). The main goal of this primary test is to check whether the parameters used for the lithosphere are compatible with its long-term stability in the absence of external perturbations, that is, to verify that in the absence of a plume the lithosphere would form a stable 'stagnant lid' on the surface of the convective mantle. Such a stagnant lid has to be dominated by heat conduction, in difference from the underlying convective mantle dominated by heat advection. The thickness of this stagnant layer, Z_{rheo}, should be equal to the thickness of the mechanically strong lithosphere, that is, to the thickness of its uppermost portion that is strong enough to prohibit convective flow above its lower boundary. As a consequence, this layer must be purely conductive. Hence, Z_{rheo} should be close to the thickness δ of the conductive lithosphere. The latter equals the sum of thicknesses of the constituent conductive layers, that is, of the crust ($h_c \sim 40$ km) and of the lithosphere mantle ($h_m = h_l - h_c$)

$$\delta = h_c + h_m \approx k_m(T_m - T_{\text{Moho}})/q_m + k_c(T_{\text{Moho}} - T_0)/q_c$$
$$= k(T_m - T_{\text{Moho}})/q_m + h_c, \qquad (4)$$

where q_m is the basal heat flux, q_c is the mean crustal heat flux, T_m is the temperature at the bottom of the stagnant lid, T_{Moho} is the temperature at Moho depth $z = h_c$. q_c and T_{Moho} are computed from

the tested thermal model of the lithosphere, q_m, T_m, k and h_c are also known. Consequently, δ can estimated from eq. (4). For example, for cratons ($q_m = 15$–20 mW m^{-2}), $\delta = 200$–250 km (Jaupart *et al.* 2007). For normal lithosphere $q_m = 30$ mWt m^{-2}, $\delta = 120$–150 km (Jaupart *et al.* 2007). δ only approximately defines the thickness of stagnant lithosphere Z_{rheo} because the latter also depends on its thermally dependent mechanical properties. For this reason, the next step is to estimate the thickness of the rheology boundary layer between the potentially strong lid and the underlying weak asthenosphere, and to ensure that the viscosity drop across this layer is compatible with the mechanical stability of the lid. In the stagnant mantle lithosphere, the effective viscosity decreases exponentially as the temperature increases with depth until this process is slowed down by rising pressure and change in the flow law, from dislocation to diffusion creep (Appendix A). The impact of temperature on the viscosity becomes nearly constant in the underlying convecting mantle as the temperature gradient becomes adiabatically small. The depth $Z_{\text{rheo}} \leq \delta$ to the zone of transition from a fast viscosity drop (predominant thermal conduction, lithosphere) to nearly constant viscosity (predominant thermal advection, upper mantle) defines the 'true' rheological and stagnant thickness of the lithosphere (see rheology envelopes shown in Fig. 3). This zone is referred to as the rheological boundary layer of thickness δ_{rheo}. This layer separates strong lithosphere ('stagnant lid') from weak underlying mantle and its thickness characterizes the mechanical stability of the 'lid'. For mantle rheology (Tables 2 and 3), the estimated characteristic temperature change for viscosity reduction in the rheology boundary layer is $T_\eta = 50$–65 K. This quantity yields a total temperature change, T_{rheo}, across the rheology boundary layer. In our model, T_{rheo} is on the order of 120–150 K (Sleep 2003b)

$$T_{\text{rheo}} \approx 2.4 T_h \approx (T_m - T_{\text{Moho}})/\theta \approx 1/A, \qquad (5)$$

where θ is Frank–Kamenetskii parameter (Solomatov 1995) defined as $\theta \approx A\Delta T$ where A (~10^{-2} K^{-1}) is 'activation parameter' for convective flow in the sublithosphere mantle (Schubert *et al.* 2001, p. 618) and $\Delta T = T_m - T_{\text{Moho}}$. The thickness of the rheological boundary layer, δ_{rheo} can be estimated as (Nyblade & Sleep 2003): $\delta_{\text{rheo}} \approx T_{\text{rheo}}\delta/T_m = 50$ km. Consequently, the characteristic stress scale, $\tau_b \sim (\delta_{\text{rheo}} g \rho_m \alpha T_{\text{rheo}}) \approx 5$–7 MPa. The value of τ_b means that if the strength of the lithosphere at its mechanical bottom ($z = Z_{\text{rheo}}$) is smaller than τ_b, it will become gravitationally unstable even in the absence of a plume or other perturbation. In this case, the lithosphere thickness will be progressively reduced by a series of mantle drippings that will remove all material, which strength is below τ_b. Using the estimate for τ_b, we can validate the initial numerical model setup by testing whether the model plate would be stagnant in the absence of a plume or folding. For the geotherms and rheology used, the strength of the model cratons is higher than τ_b down to the depth of 200–250 km. Depending on its age (60–300 Ma), the strength of the younger lithosphere is higher than τ_b down to the depth of 100–150 km. For $\tau_b \sim 5$–7 MPa and typical tectonic strain rates of 10^{-14}–10^{-15} s^{-1}, the effective mantle viscosity is on the order of 10^{20}–10^{21} Pa s, which falls within the commonly accepted range for the sublithosphere mantle.

5 EXPERIMENTS AND RESULTS

5.1 Plume instability below continental lithosphere, in the absence of far-field compression

Summary of the experiments shown in the figures is presented in Table 4. We first have conducted a series of experiments with a

Table 4. Summary of the experiments shown in the figures.

Thermomechanical age of the lithosphere (Ma)	Mantle geotherm (cold/hot)	Lateral boundary conditions (compression or no)	Plume diameter d (km)	Compression rate (mm yr⁻¹)	Resolution (element size, km)	Thermodynamic coupling	Figures
60	h	No	200	NA	5 × 5	No	Fig. 4(a)
150	h	No	200	NA	5 × 5	No	Fig. 4(b)
150	h	No	200	NA	2.5 × 2.5	No	Figs 4(c) and (d)
300	h	No	200	NA	5 × 5	No	Figs 5(a) and (b)
300	c	No	200	NA	5 × 5	No	Figs 5(c) and (d)
300	c	Yes	200	0	5 × 5	No	Figs 5(e) and (f)
300	h	No	100	NA	5 × 5	No	Figs 7(a) and (b)
1000	h	No	200	NA	5 × 5	No	Figs 6(a) and (b)
60	h	Yes	0	30	5 × 5	No	Fig. 8
300	h	Yes	0	30	5 × 5	No	Figs 9(a)–(c)
150	h	Yes	200	30	5 × 5	No	Fig. 10(a)
150	c	Yes	200	30	5 × 5	No	Fig. 10(d)
300	h	yes	200	30	5 × 5	No	Fig. 10(b)
1000	h	Yes	200	30	5 × 5	No	Fig. 10(c)
300	h	No	200	NA	5 × 5	Yes	Figs 11(a) and (b)

single ($d = 200$ km) plume upwelling below lithospheres of different thermotectonic age (from 60 to 1000 Ma, Figs 4–6). These experiments were then repeated with a two-times smaller plume ($d = 100$ km, Fig. 7). Additional high-resolution experiment has been conducted with a two times higher numerical resolution to (1) check the applicability of the results obtained with standard resolution (Fig. 5g).

Fig. 4(a) shows the experiments of PLI in case of a very young and weak (60 Ma) lithosphere assuming a quartz-dominated rheology for the entire crust. These experiments show that the ascending plume head first (time < 1 Myr) produces large scale ($\lambda > 1000$ km) relatively small amplitude a ($a < 1$ km) uplift superimposed by short-wavelength tensional and locally compressional crustal instabilities ($\lambda < 50$ km, $a < 100$ m). This deformation is soon relayed (after 1 Myr) by a higher amplitude tectonic scale uplift ($\lambda = 250$–300 km, $a \sim 2$ km) superimposed by amplified short-wavelength crustal deformation ($\lambda < 50$ km, $a \sim 300$ m). Various wavelengths do not always coincide in time. The smallest observed wavelength of 30–40 km refers to the initial small-offset periodic faulting in the brittle crust, which spacing is proportional to 1–2 thickensses of the brittle layer. The initial closely spaced faults die out when the deformation localizes at the inflexion points of major synclines and anticlines. These initial faults are well resolved in the high-resolution experiment shown in Figs 4(c) and (d). The localized topography growth continues for the next several Myr yielding final amplitudes on the order of 5 km. This topography amplitude, h, obviously results from the important positive buoyancy of the plume head associated with its high thermal and chemical density contrast with the surrounding material (part of which is the light crust at the initial stages of crustal thinning), that overshoots the negative topography that would be produced by plume-induced crustal thinning. Simple isostatic estimates suggest that 3–3.5 of 5 km of positive topography is due to plume buoyancy (plume density contrast $\Delta\rho_p$ with averaged (crust and mantle) lithospheric rock is $\Delta\rho_p \sim 100$–120 kg m⁻³), which overshoots about 6 km of negative syn-rift subsidence, h_i, that would be produced by crustal thinning (h_i strongly depends on crustal strength and the availability of the basin infill and its assumed density, ρ_s, that may vary from 0 in case of no infill to 2700 kg m⁻³ in case of dense infill): $h_b \approx \Delta\rho_p w / \rho_l$, where h_b is the buoyant part of the uplifted topography and w is the vertical deflection of the base of the lithosphere due

to the intrusion of the plume head ($w \sim 100$ km for the middle experiment of Fig. 4a). The amplitude of maximal would-be-negative subsidence h_i due to the crustal thinning can be estimated from the classical McKenzie (1978) formulae that assumes local isostasy: $h_i = h_l(1 - \beta^{-1})\{h_c h_l^{-1}(\rho_m - \rho_{cu})[1 - 0.5\alpha T(h_l)h_c h_l^{-1} - 0.5\alpha\rho_m T(h_l)]\}\{\rho_m[1 - \alpha T(h_l)] - \rho_s\}^{-1}$, where β is the lithosphere thinning factor, which is on the order of 6–8 for the last snapshot of the Fig. 4(a), and $T(h_l)$ is the initial temperature at the depth h_l [$T(h_l) = 1330\,°C$ is the temperature at the thermal bottom of the lithosphere]. The large-scale dynamic topography is thus responsible for less than 1.5 km of the remaining topography uplift. Local isostatic relations do not hold for topographic features with wavelengths smaller than 1000 km in case of stronger lithospheres/smaller stretching factors; in this case there is an important contribution from non-lithostatic compensation of the surface topography associated with its flexural strength. Actually, even in the case of the 'weak' experiment shown in Fig. 4(a), the uppermost 5 km of surface topography rapidly cools down to less than 300 °C and becomes brittle. The 'non-dynamic' part of topography is then maintained over important time spans due to the strain-rate and temperature independent brittle-elastic strength of near-surface material: the brittle strength of the rocks is ~ 0.6–0.8ρ g × (5000 m) + 20 MPa $\sim$ 120–150 MPa (Goetze & Evans 1979), the weight of the 'non-dynamic' 3.5 km of topography is less than 120 MPa. If this topography was not 'strong' enough, it would have been flattened by gravity driven flow in less than 1–2 Myr. Higher than 5 km topography amplitudes are physically possible in case of large-wavelength uplifts. In that case the topography slopes should not exceed the internal friction angle of the surface rock, which limits the maximal amplitude of short-wavelength deformation. To preserve such topography, the effective viscosity μ of the subbrittle layers should be high enough (e.g. $>10^{23}$ Pa s) to sustain topography loads: $\rho g h < \mu\dot\varepsilon_{yy}$, where $\dot\varepsilon_{yy}$ is vertical strain rate, on the order of 10^{-15}–10^{-13} s⁻¹ (typical tectonic strain rate). High topographies are unlikely for pure PLIs but may be reproduced if the PLI are associated with tectonic folding of strong lithosphere.

As its spreads laterally, the plume head erodes a significant part of the mantle lithosphere provoking, at 4.5–5 Myr, whole-scale mantle lithosphere down thrusting. At 5 Myr the crust is thinned by a factor of 3–5, yielding extreme rifting, continental break-up and onset of oceanization above the plume head. It is also noteworthy
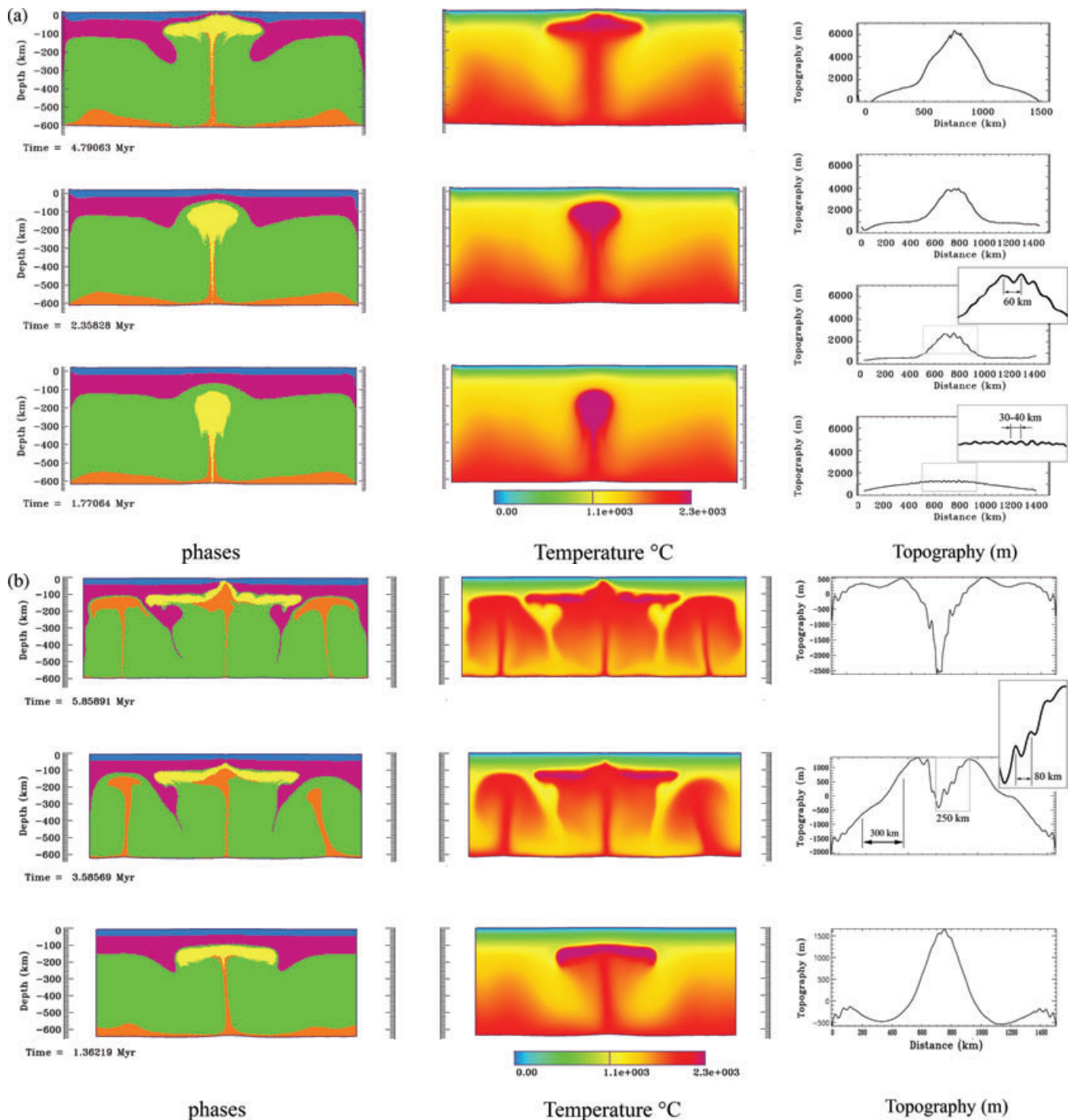
Figure 4. Experiments on interaction of a plume with young continental lithosphere, no compression. (a) Plume and very young 60 Ma old lithosphere. Shown are the material phases (left-hand panel), temperature distribution (centre panel) and topography (right-hand panel) during the first stages of plume emplacement. The colour code: blue – upper and lower crust; purple – lithosphere mantle; green – sublithosphere mantle; yellow – plume; orange – marker layer at the bottom of the mantle, with the same properties as the mantle. The case shown here refers to a very weak hot plate that is not representative for the present-day lithospheres. It could, however, be a plausible scenario for early Archean plates. (b) Plume and young (150 Ma old) lithosphere that has a thermal structure compatible with that of the European Alps. Other notations as in (a). (c) High resolution (size of elements 2.5 km × 2.5 km) experiment corresponding to the standard resolution experiment from (b) (150-Ma-old lithosphere). Other notations as in (a). (d) Left-hand panel: strain rate distributions in high-resolution experiment demonstrate brittle faulting in the crust and in the uppermost lithosphere mantle. Several populations of faults are generated: small-scale small-wavelength small offset initial faulting with spacing (30–40 km) proportional to the thickness of the brittle layer (these faults die out and periodically reverse their tilts), and major persisting faults associated with large-scale deformation. Right-hand panel: time averaged (5 Myr) high-pass filtered (500 km cut-off wavelength) power spectrum of surface topography showing dominating wavelengths of 350, 250, 80, 60 and 30 km.
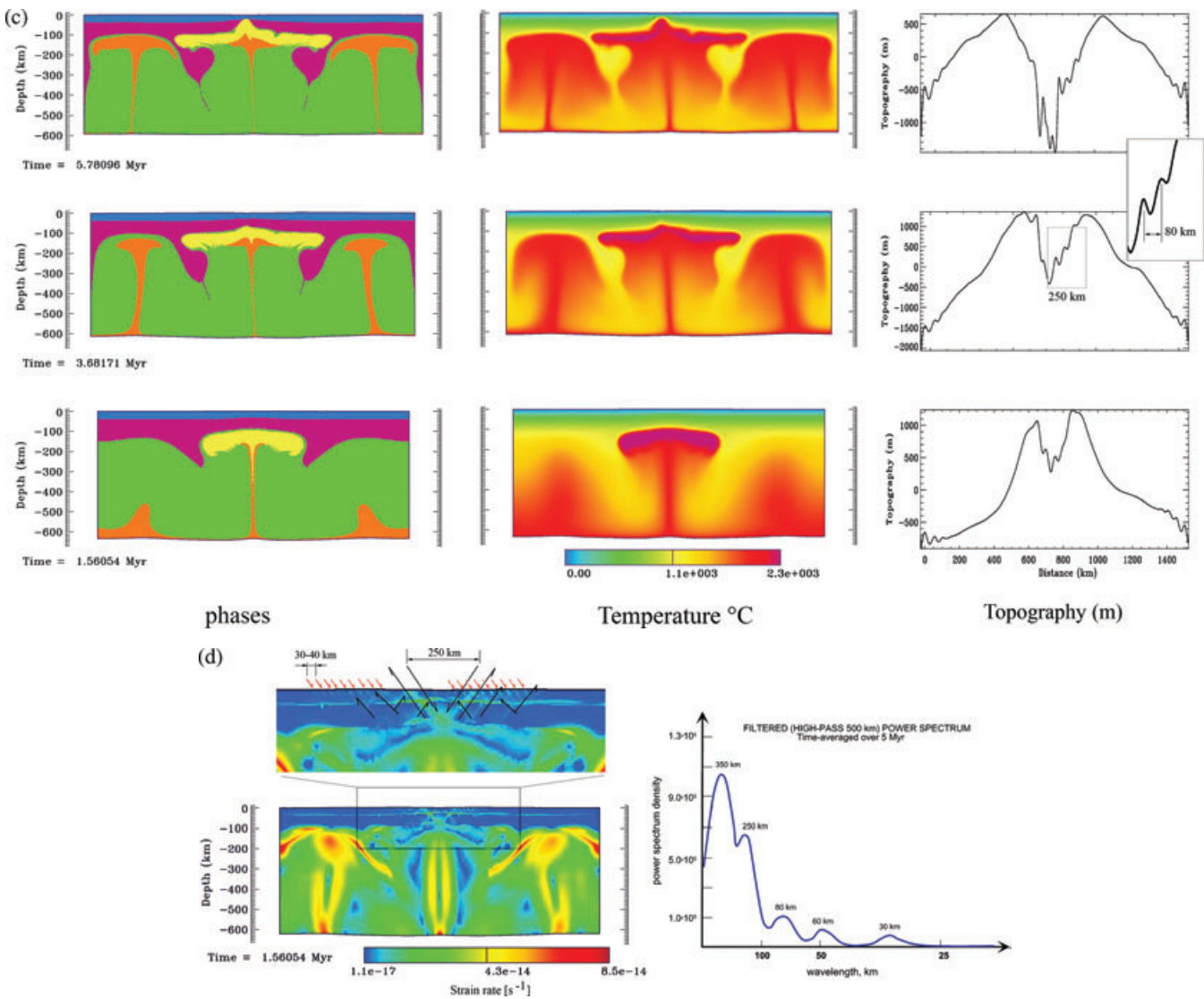
Figure 4. (*Continued.*)

that the laterally spreading plume head laterally splits the mantle lithosphere in two parts one, which is down thrusted whereas the other, thinned one, remains above the plume head. The case considered in Fig. 4(a) is hardly applicable to the present-day lithospheres that are mostly stronger and colder than a 60 Ma old plate. This could be, however, a more realistic scenario for early Archean plates.

Fig. 4(b) shows PLI experiments for 150 Ma old lithosphere, which is geotectonically more representative than the 60-Ma-old lithosphere assumed in the experiment of Fig. 4(a). All other parameters are identical to those chosen for the experiments of Fig. 4(a). In this experiment, we observe that the plume head intrudes at a large scale in the lithosphere and produces rifting with flexural-scale rift shoulders. The topography has a large-scale uplift of 600 km wide, with amplitude of up to 3–4 km. Inside the uplifted area (snapshot at 3.5 Myr, Fig. 4b) there is a 2 km deep rift basin of 250–300 km width. The flattened plume head exhibits large strain zones concentrated at the lithosphere–plume boundary. The plume continued spreading at 5.6–6 Myr. At this stage the plume moved further toward the surface, provoked a subduction-like down thrusting of the mantle lithosphere to 400 km depth and produced a large

wavelength uplift in an area of >1000 km wide, with an vertical amplitude of 3 km overprinted by a 300 km wide rift-type basin with a depth of about 2 km.

High-resolution plume experiment (Figs 4c and d). We have additionally conducted experiments with increased resolution (twice better than standard, i.e. 2.5 km × 2.5 km) using the setup of the experiment from Fig. 4(b) (150 Ma old lithosphere). The results (Fig. 4c) are largely consistent with those obtained for standard resolution (Fig. 4b) but provide a better resolution for small-scale brittle faulting in the uppermost lithosphere, in particular for small-scale small offset periodic faulting that develops at the initial stages of PLI (Fig. 4d). This faulting is responsible for smallest topography wavelengths of 30–40 km. Small-scale small offset initial periodic faulting is typical for extension or compression of elasto-plastic layers overlying low-strength viscous media (lower crust, asthenosphere). As could be expected for the rheological parameters used for this experiment, the wavelength of the initial periodic faulting is on the order of 1–2 brittle layer thickness (e.g. Gerbault *et al.* 1999: Bellahsen *et al.* 2003). These faults die out later, when the brittle deformation starts to localize at the inflection points of the well-developed synclines and anticlines.
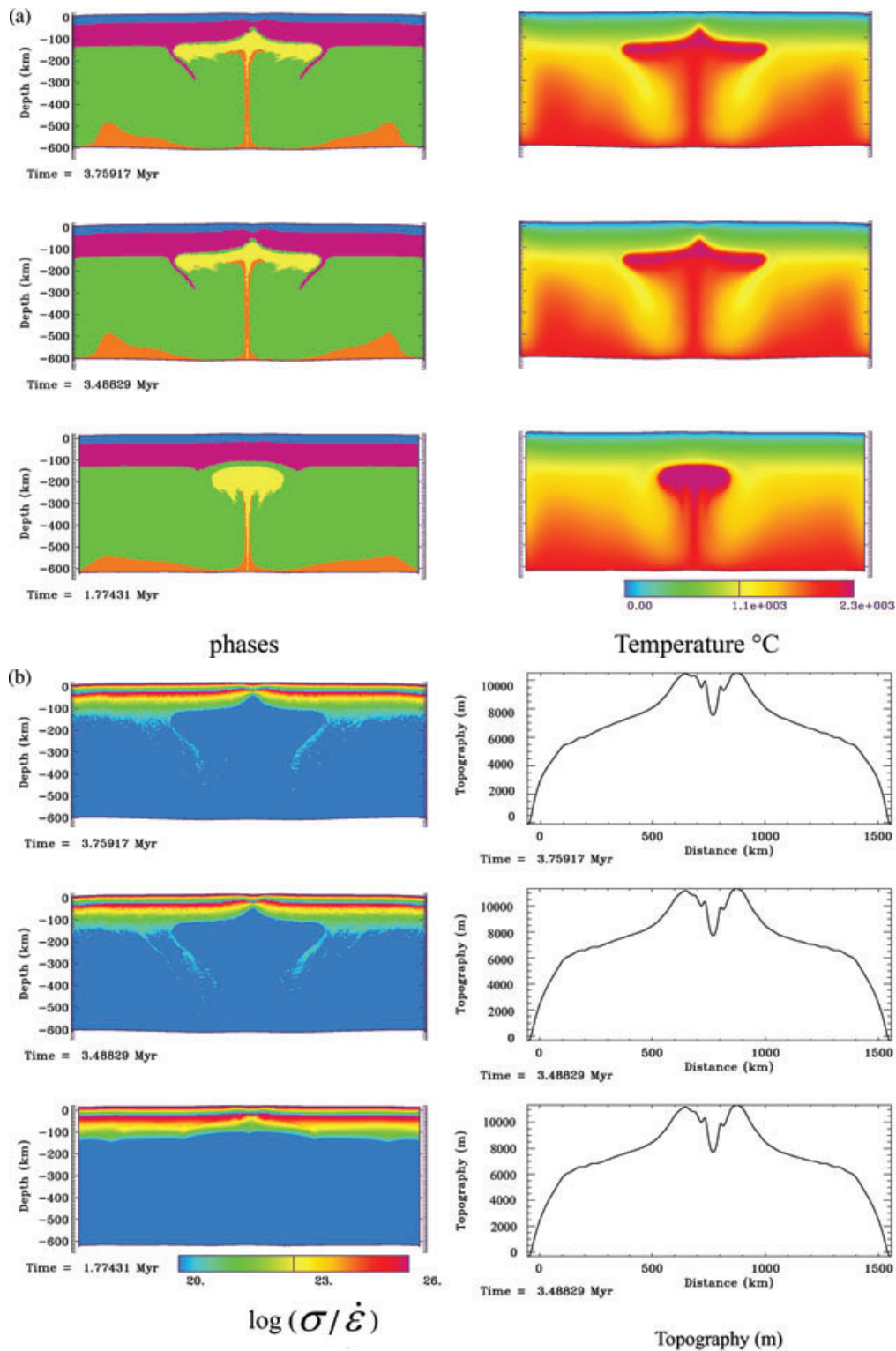
Figure 5. Experiments on interaction of a plume with old lithosphere (300 Ma), no compression. (a) Phase (left-hand panel) and temperature (right-hand panel) distribution during the first stages of plume emplacement, 'hot' geotherm (2000 °C at 650 km depth), open lateral borders. (b) Effective viscosity (ratio of second invariant of stress to that of strain rate, left-hand panel) and surface topography evolution (right-hand panel) for the experiment of (a). N.B. A viscoelastoplastic rheology is used, the effective viscosity (= stress to strain rate ratio) is computed to evaluate the effective strength, that is, the use of this term does not imply that the material is viscous. (c) Phase (left-hand panel) and temperature (right-hand panel) distribution in case of 'cold' mantle geotherm (corresponding to the assumption of whole mantle convection whole mantle convection with $T = 1700$ °C at 650 km depth), open lateral borders. (d) Effective viscosity (ratio of second invariant of stress to that of strain rate, left-hand panel) and surface topography evolution (right-hand panel) for the experiment of (c). N.B. A viscoelastoplastic rheology is used, the effective viscosity (= stress to strain rate ratio) is computed to evaluate the effective strength, that is, the use of this term does not imply that the material is viscous. (e) Phase and temperature distribution in case of the 'cold' mantle geotherm (same as in the experiment in (c and d) assuming fixed lateral borders. (f) Effective viscosity and surface topography evolution for the experiment shown in (e).
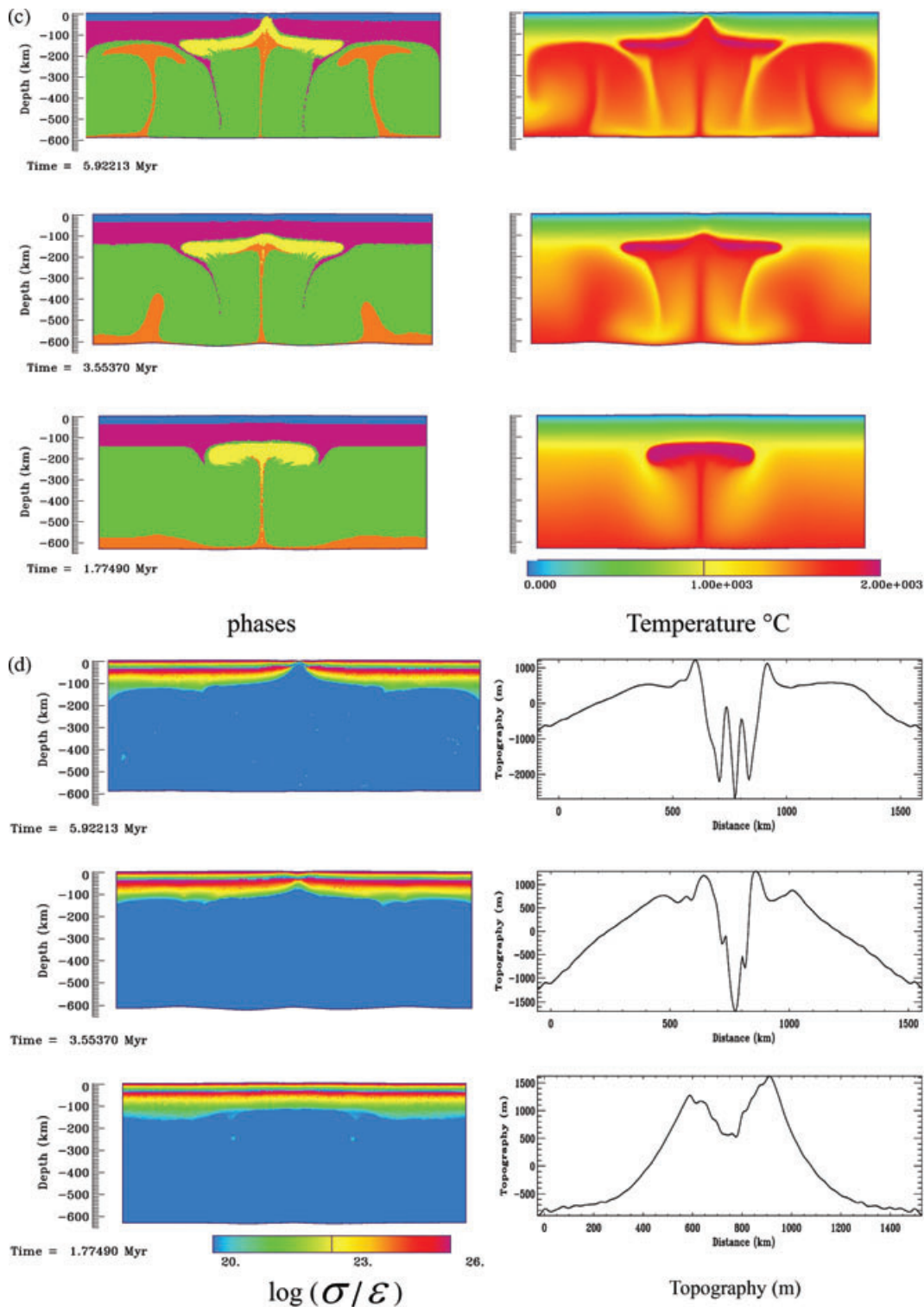
Figure 5. (*Continued.*)

Fig. 5 shows the experiments for 300 Ma lithosphere conducted both for a 'hot' mantle geotherm (double layer convection concept, 2000 °C at 650 km depth, Figs 5a and b) and a 'cold' mantle geotherm (whole mantle convection concept, 1700 °C at 650 km depth, Figs 5c–f). As can be seen, compared to the experiments with young 60 Ma lithosphere in case of a 'hot' mantle geotherm, the plume head still produces significant mantle down thrusting but lithospheric thinning above the plume head is more localized than in the case of 60 Ma lithosphere. The topographic features are characterized by tectonic-scale uplift ($\lambda = 400$–500 km, amplitude, $a \sim 2$ km) with a smaller scale crustal wavelength. In contrast with the previous case, major subsidence surrounded by uplifted rift shoulders is observed right above the centre of the plume head. In case of a 'cold' mantle geotherm (Figs 5c and d) some minor
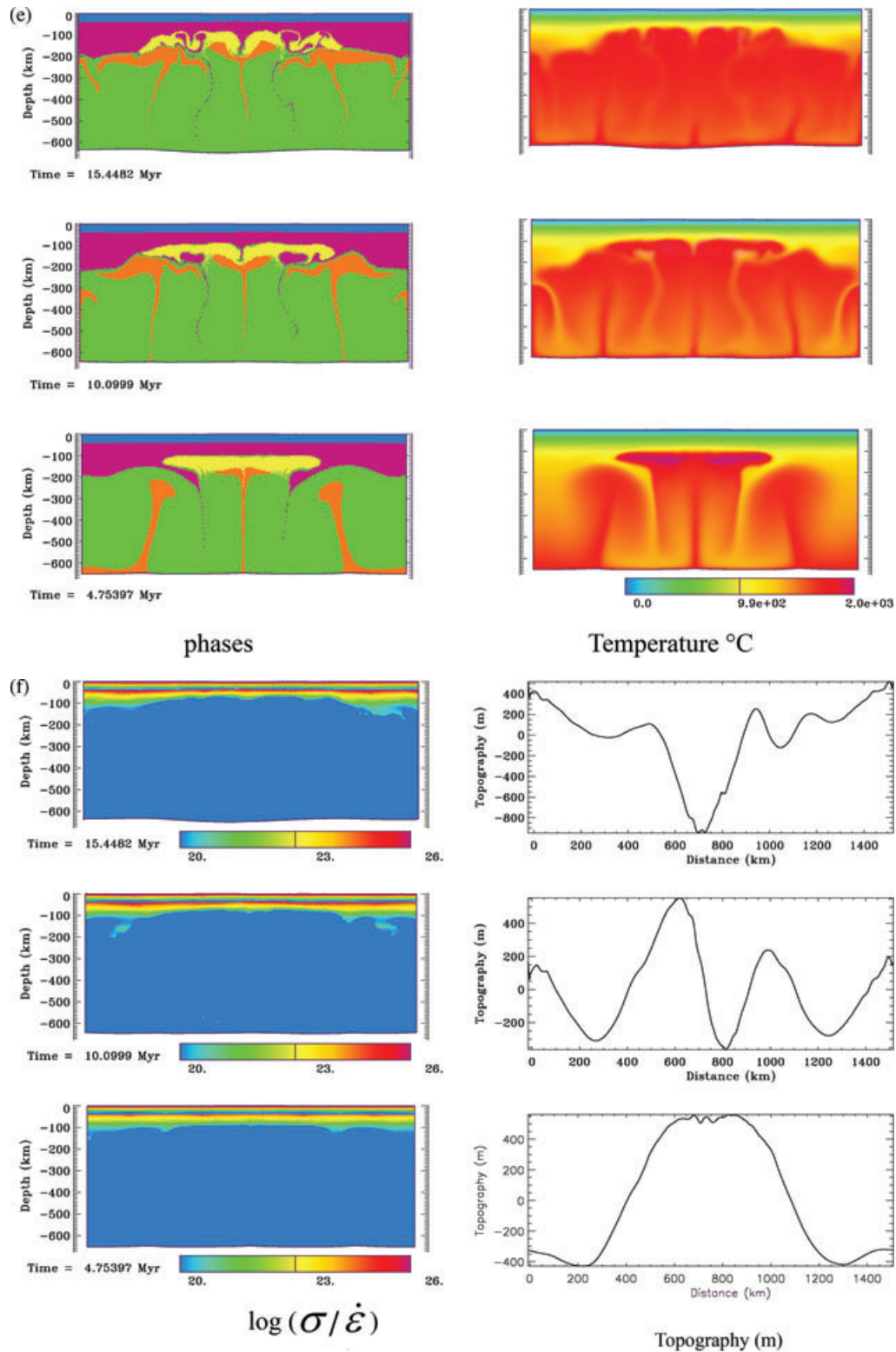
phases

Temperature °C

$\log\left(\sigma/\dot{\varepsilon}\right)$

Topography (m)

Figure 5. (*Continued.*)

differences occur with the case of the 'hot' geotherm, but the main features of PLI are basically the same. Figs 5(e) and (f) shows a case identical to that of Figs 5(c) and (d) but for fixed lateral boundary conditions. This experiment explores the situation when the deformation of the lithosphere is constrained by far-field tectonic forces

(intermediate state between pure PLI and PLI occuring simultaneously with tectonic compression/folding considered in the following sections). In this case, the mantle lithosphere becomes more gravitationally instable due to smaller Péclet numbers. As a result, initially underthrusted mantle lithosphere material becomes highly

phases

Temperature °C

$$\log(\sigma/\dot{\varepsilon})$$
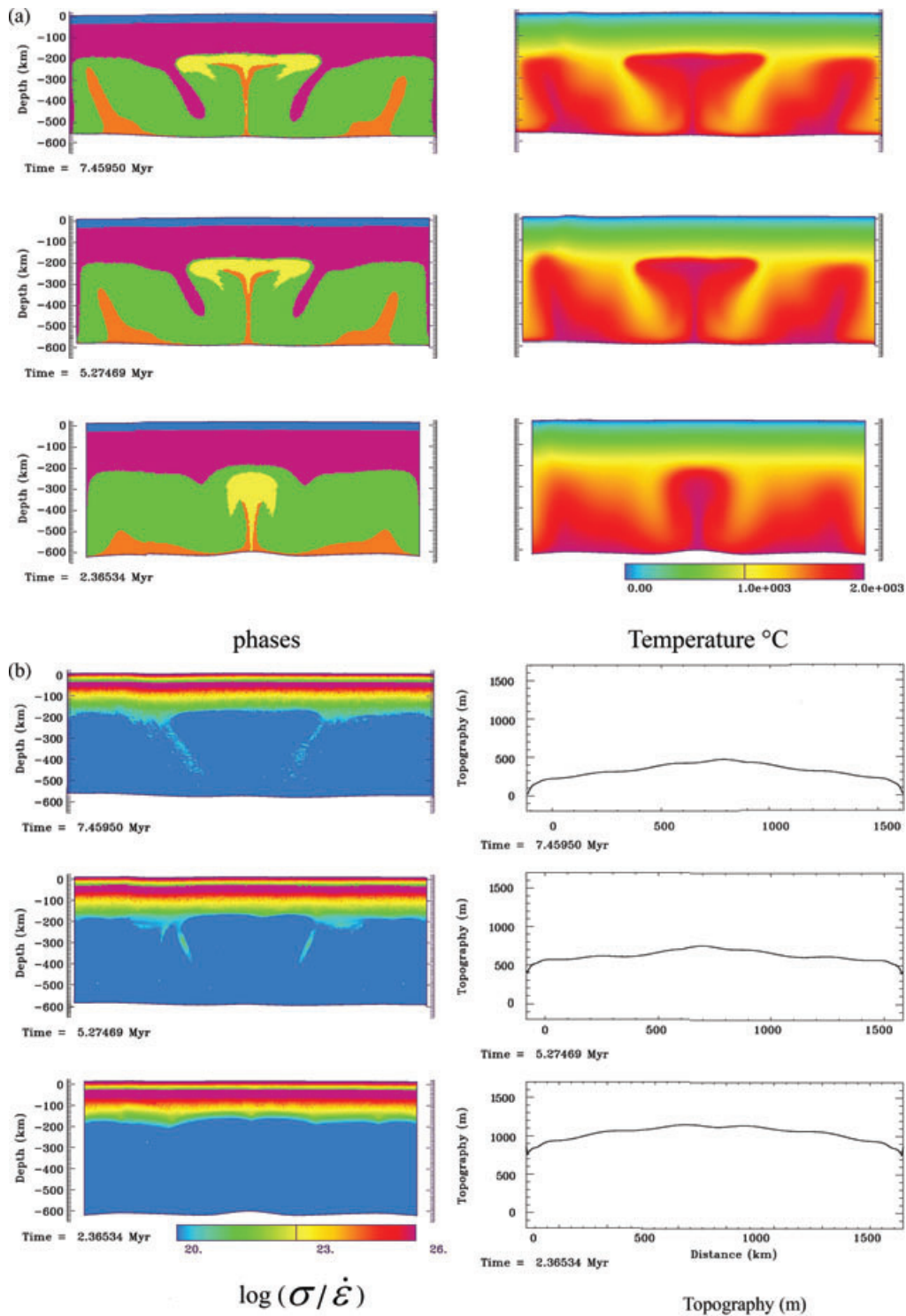
Topography (m)

Figure 6. Experiments: plume and cratonic lithosphere (1000 Ma), no compression. (a) Phase (left-hand panel) and temperature distribution (right-hand panel) during the first stages of plume emplacement. (b) Effective viscosity (left-hand panel) and surface topography evolution (right-hand panel). N.B. Viscoelastoplastic rheology is used, the effective viscosity is computed to evaluate the effective strength and does not necessarily imply that the material is viscous.

gravitationally unstable, specifically at its base (the material makes several up-and-down turns with characteristic scale–demultiplication of the instabilities).

As the age of the lithosphere increases (Fig. 6, age 1000 Ma), the mantle-downthrusting provoked by the plume head remains very significant but the amplitude of the surface expression is smaller

(0.5 km) while its wavelength is larger ($>$600 km). Periodic surface undulations with a wavelength of 300 km (produced by very strong crust) are also observed.

Experiments with a smaller ($d = 100$ km, Fig. 7) plume demonstrate that even a little 'baby' plume can have a noticeable impact on the mantle lithosphere (thermomechanical erosion of mantle
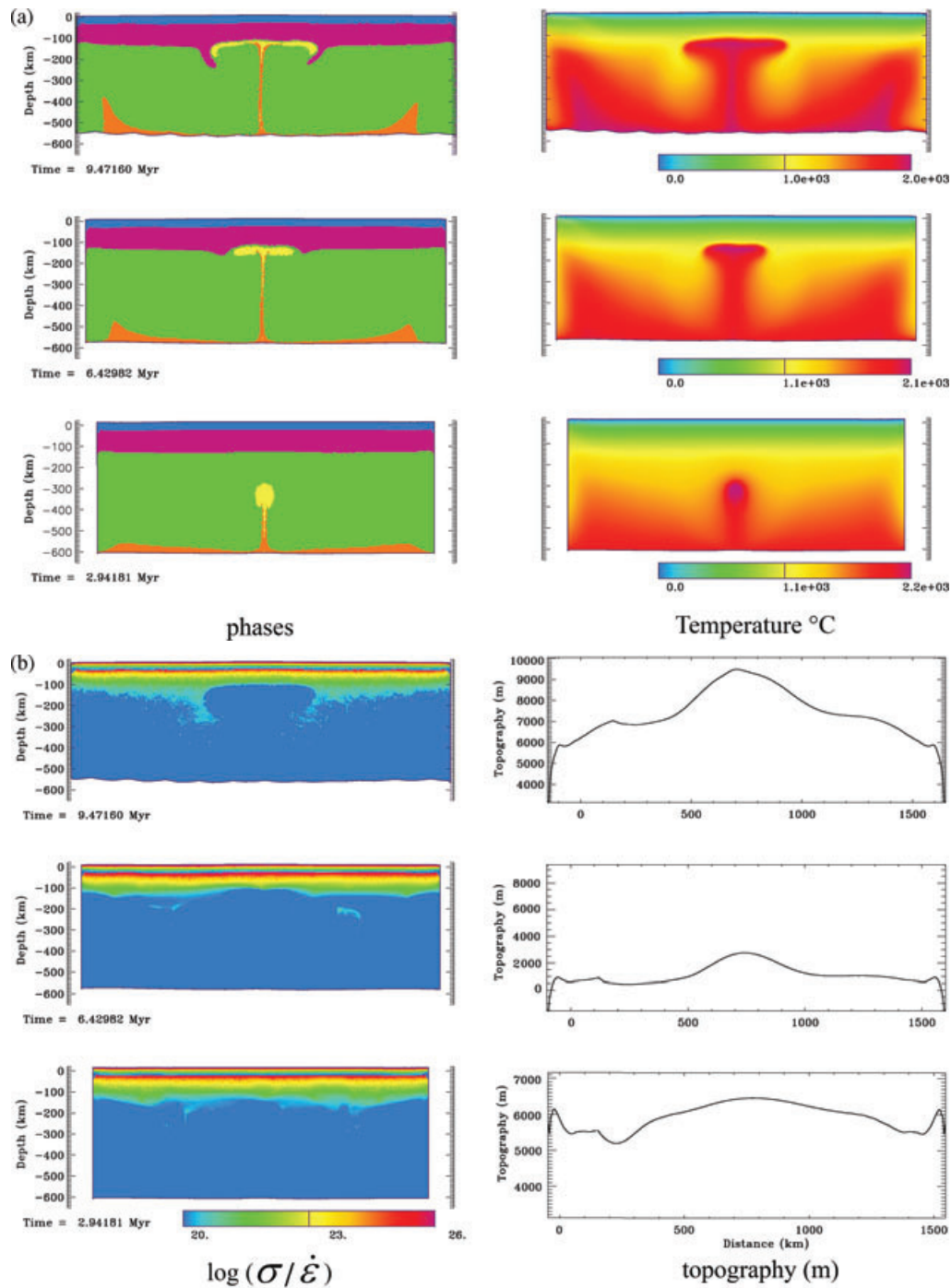
Figure 7. 'Baby' plume experiment: Small (100 km in diameter) plume below 300-Ma-old lithosphere, no compression. (a) Phase (left-hand panel) and temperature distribution (right-hand panel) during the first stages of plume emplacement. (b) Effective viscosity (left-hand panel) and surface topography evolution (right-hand panel). N.B. Viscoelastoplastic rheology is used, the effective viscosity is computed to evaluate the effective strength and does not necessarily imply that the material is viscous.

lithosphere, its down thrusting to important depth) and surface topography (tectonic scale undulations with wavelengths similar to the large plume experiments and with amplitudes of up to 2000 m). It confirms that the final surface wavelengths are controlled by the mechanical properties of the lithosphere. It shows also that the thermal anomaly associated with the plume head (Fig. 7a) is flattened and highly thinned and stretched along the lithosphere-asthenosphere interface making it probably unresolvable in terms of its tomographic expression. In contrast, the tail appears to be characterized

by a more pronounced vertical thermal and compositional anomaly that might be better resolved in seismic tomographic studies (see for a comparison Fig. 2b, top panel).

5.2 Folding instability in continental lithosphere in presence of far field compression

The next series of experiments address the development of a folding instability in the lithosphere, in the absence of mantle plumes
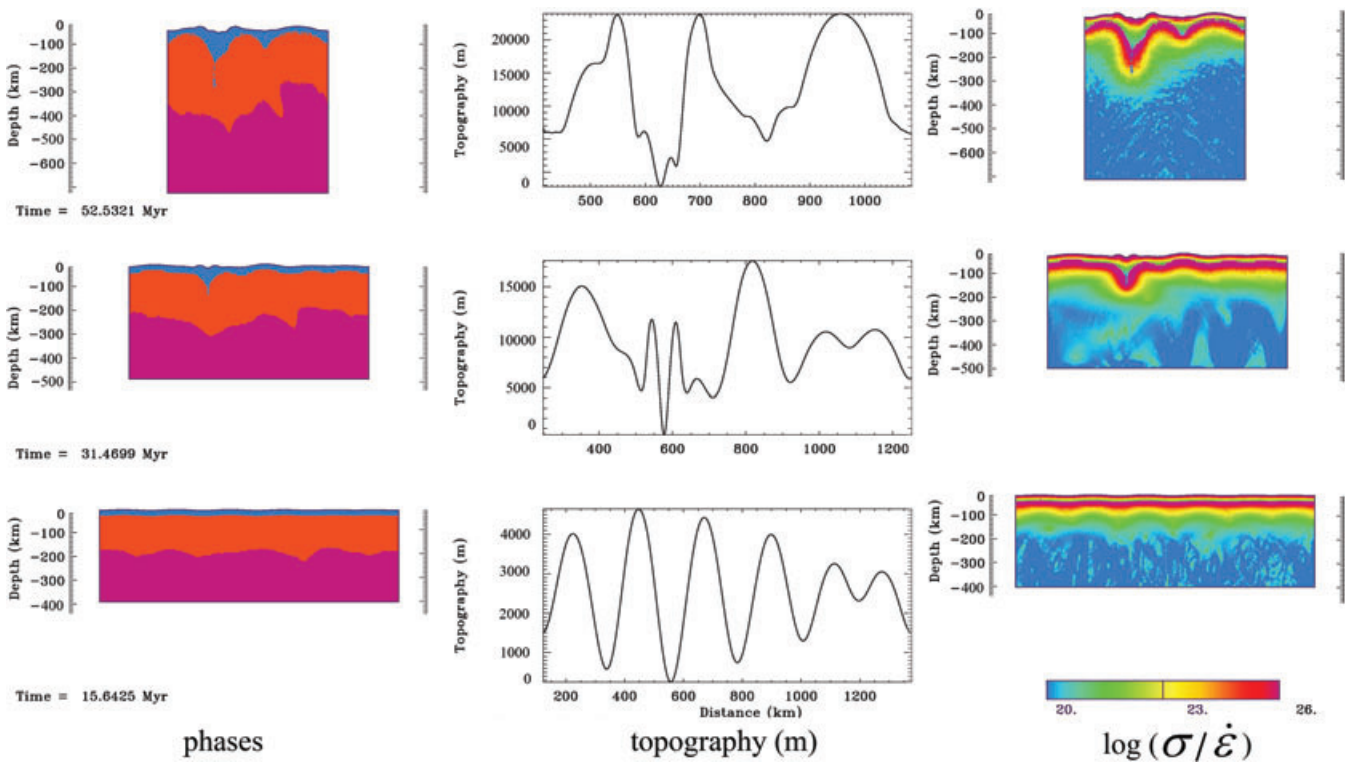
Figure 8. Experiments for folding of very young (60-Ma-old) lithosphere (convergence rate of 3 cm yr^{-1}). Phase distribution (left-hand panel), topography (centre panel), effective viscosity (right-hand panel).

but with the other conditions identical to the experiments of Section 5.1.

Fig. 8 shows the results of the experiments for very young 60-Ma-old lithosphere compressed at a slow rate of 3 cm yr^{-1}. In this case, some strongly decoupled low-amplitude short wavelength (mantle wavelength, $\lambda = 100$ km) folding developed leading to crustal thickening above a synclinal mantle fold. At later stages, harmonic folding is followed by mega-folding (Cloetingh *et al.* 1999; Burg & Podladchikov 2000), and these mantle synclines develop in a mode resembling symmetric subduction. For lower convergence rates folding does not develop due to the low Péclet number of the system (leading to heat diffusion and weakening of folds). Basically the same results were obtained for 150-Ma-old lithosphere. These experiments could be relevant for offshore parts of the Norwegian margin not affected by plume activity.

Folding is well developed for medium age lithosphere (300 Ma, Fig. 9). In this case it develops for all, slow (1.5 cm yr^{-1}), high (6 cm yr^{-1}) and intermediate (3 cm yr^{-1}) convergence rates, with long mantle wavelengths ($\lambda = 360$ km) and high surface amplitudes (2000 m after 10 Myr; this case compares well with Iberia (see Lozano *et al.* 2008) or Western Goby and the Ferghana basin in Central Asia (Burov *et al.* 1993; Burov & Molnar 1998). At late stages (10–26 Myr after the onset of shortening for 3 cm yr^{-1} or 20–50 per cent of shortening), folding becomes aperiodic, leading to mega-folding (Cloetingh *et al.* 1999; Burg & Podladchikov 2000) and subsequent formation of high-amplitude crustal down-warps (Fig. 9b). In this case, the amplitude of vertical movements may reach 20 km (± 10 km) or even more. Actually, such high amplitudes of vertical motions are observed in a number of sedimentary basins such as the South Caspian basin (Guest *et al.* 2007) and the Barents Sea (Faleide *et al.* 2008; Ritzmann & Faleide 2009). However, in nature it may be relatively rare for folding to continue for periods in

excess of 10 Myr. More common is that at certain moment various localizing factors lead to localization of deformation along single major fault zones (Cloetingh *et al.* 1999; Gerbault *et al.* 1999).

For the cratonic case (1000 Ma lithosphere), two wavelengths are observed ($\lambda = 150$ and 500 km) and decoupled crustal–mantle folding occurs. These experiments predict very large surface amplitudes on 10 km scale in the case of a high (6 cm yr^{-1}) convergence rate. For intermediate (3 cm yr^{-1}) convergence rates, wavelengths are about $\lambda = 560$–600 km (no crust-mantle decoupling) with amplitudes on the scale of 5000 m. For low convergence rates folding was not significant.

5.3 Simultaneous PLI and folding instability in continental lithosphere in presence of far field compression

As can be seen from the previous experiments, it appears in general that no folding occurs in case of very low convergence rates (<1.5 cm yr^{-1}). For high and medium convergence rates, classical high amplitude folding is induced in intermediate (300 Ma) and old cratonic lithosphere (1000 Ma). This might provide an explanation why folding develops preferably in Paleozoic massifs (e.g. the Armorican Massif) or otherwise prefers pre-existing sedimentary basins (Paris Basin; Pannonian Basin). To produce folding in young lithosphere and for low convergence rates for all lithospheric ages, it appears that an interaction with plume activity is required. To explore this further, is in fact the objective of the experiments of this section (Fig. 10).

To investigate the interactions between PLI and folding instability, we have repeated the experiments of Section 5.2 additionally assuming simultaneous development of a plume instability, as in the experiments of Section 5.1. In view of space restrictions, we mainly show here the results of experiments for PLI and folding
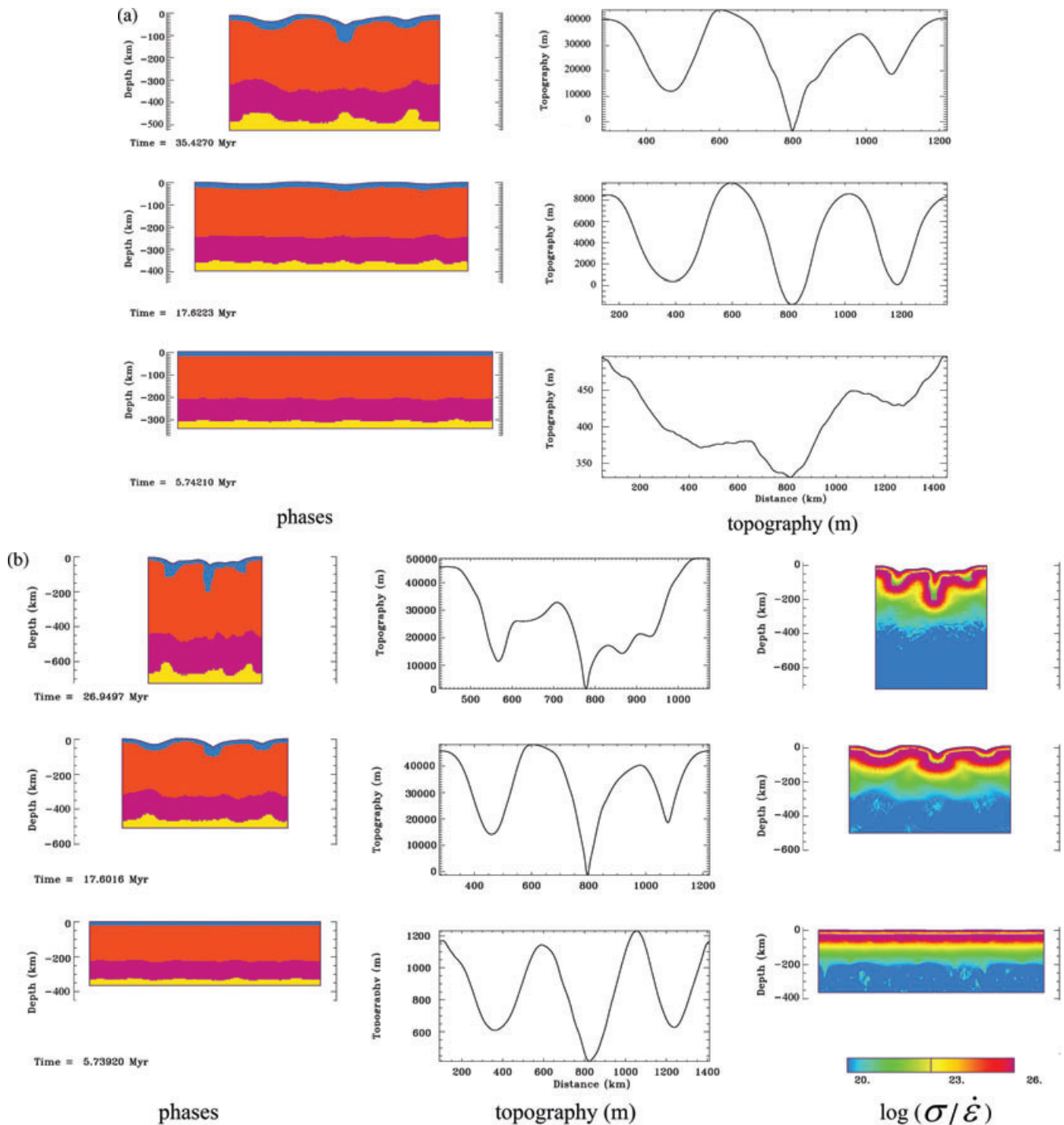
Figure 9. Experiments for folding of old lithosphere (300 Ma). (a) Convergence rate of 1.5 cm yr^{-1} (material phases and topography). See Fig. 7 for figure conventions. (b) Convergence rate of 3 cm yr^{-1} (material phases, topography and effective viscosity). See Fig. 8 for figure conventions. (c) Convergence rate of 6 cm yr^{-1} (material phases, topography). See Fig. 7 for figure conventions.

at a 3 cm yr^{-1} convergence rate and lithospheric ages from 150 to 1000 Ma (Fig. 10). In case of very young lithosphere (60 Ma), the experiments show that folding is overprinted by plume impact and the results of the experiments resemble those of the Section 5.1 for an identical age of the lithosphere.

The main differences from pure PLI deformation are most evident in the case of strong lithospheres (thermotectonic age >150 Ma). Starting from thermotectonic ages on the order of 100–

150 Ma (Fig. 10a), the topography starts to develop in a folding mode, with initially strong bi-harmonic features (crustal folding at 70 km wavelength superimposed on larger 300 km wavelength of mantle folding). The initiation of plume ascent is retarded (about 1 Myr) compared to pure PLI, but when the plume head starts to approach the base of the lithosphere, folding patterns become highly perturbed, which is initially expressed by an increase of the mantle wavelength to almost 500 km. After 5 Myr PLI like deformation
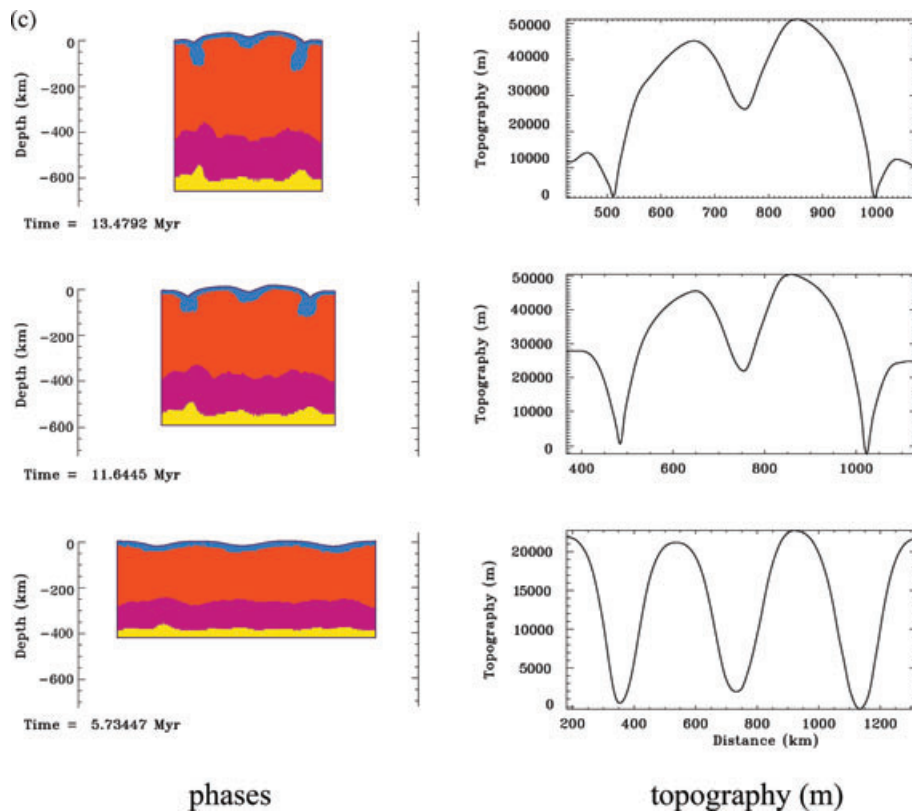
Figure 9. (*Continued.*)

dominates but the narrow rift basin forming above the plume head becomes highly asymmetric, with a high rift flank on one side and a three times smaller rift flank on the other side. Also the mantle deformation wavelength tends to grow, except for the central syncline, which shrinks. This growth can be interpreted as a result of phase mismatch between the folding and PLI-induced wavelength. By changing the initial plume location by one half of the folding wavelength we verified that PLI can also amplify the amplitude of the initial folding wavelength, without changing it. The differences from pure PLI deformation are also pronounced in case of a 300 Ma lithosphere (Fig. 10b). In this case, folding first develops almost in the same way as in the pure folding case (Section 5.2) but the surface wavelength appears to be soon affected by the plume. As in the case of 150 Ma old lithosphere, the initialization of the plume is retarded by about 1 Myr. The position of the points of maximal amplitude is shifted compared with the pure folding case, and one of them coincides with the location of the plume head. The observed wavelength is $\lambda = 400$ km, slightly larger than in the case of pure folding. In case of the convergence rate of 3 cm yr^{-1}, dramatic surface uplift of 2000–3000 m with a wavelength of $\lambda = 400$ km is observed on top of the plume at about 2 Myr. At later stages (5 Myr), the surface elevation flattened out yielding lower amplitude folding of wavelengths of $\lambda = 300$ km. Folding then starts to dominate with a topographic low in the surface expression at the site of a former topographic high induced at the first stage by the plume. In case of very strong lithosphere (1000 Ma, Fig. 10c), folding dominates and the plume impact is not expressed in the surface topography. We note, however, a shift of folding deformation towards the areas that are most affected by thinning of the lithosphere by thermal and mechanical erosion caused by the plume. Down thrusting of the plume and lithosphere mantle material is well expressed in all

cases so that the deformation of the bottom of the lithosphere was always plume-dominated. Similar tendencies are observed in case of a 'cold' whole mantle convection geotherm (Fig. 10d), except that the development of the rift basin is attenuated, and the development of mantle down-sagging above the plume head is amplified. In case of a 'cold' mantle geotherm, a main syncline tends to localize above the plume head, as in the case of a 'hot' geotherm shown in Fig. 5(a), whereas the overall fold pattern is asymmetric.

In case of a lower convergence rate (1.5 cm yr^{-1}), the plume produces large-scale uplift with a magnitude of 1.6 km above the plume head and a large 1000 km wide area is affected by plume impingement. The initial uplift flattens out after about 8 Myr, and then small amplitude folding with wavelengths of $\lambda = 250$ km and small (100–300 m) vertical displacements develop. This stage could be interesting in view of subtle intraplate deformation commonly observed in intraplate settings (e.g. Siberia), traceable through river drainage patterns (Allen & Davies 2007). Interestingly, plume material appears to be attracted by folding in Variscan-type massifs: maybe these massifs represent the optimum in terms of rheology, which is not too strong yet but still capable to fold.

For all convergence rates, the plume has created an initial surface uplift of about 1000 m (after 2–3 Myr) that flattened out to smaller levels of 200 m.

5.4 General observations

Summarizing all experiments on PLI-folding interactions, we can conclude that: (1) in case of young lithospheres (<150 Ma), PLI overprints folding but the PLI-associated patterns tend to become asymmetric; (2) in case of strong lithospheres (>300 Ma), folding may dominate over PLI-induced patterns but the plume may
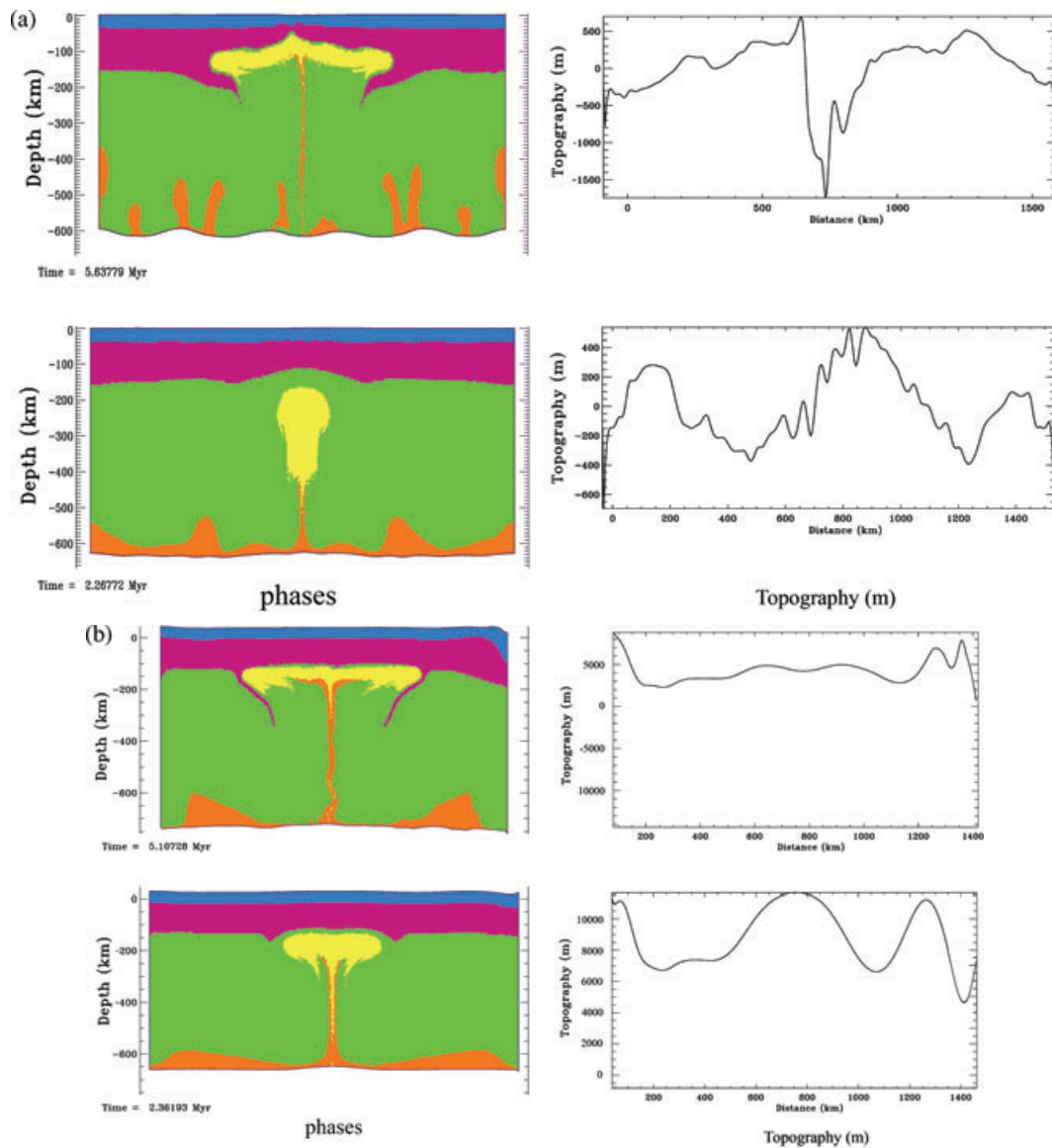
Figure 10. (a) Experiments on simultaneous PLI and folding of 150 Ma old lithosphere with 'hot' mantle geotherm (= 2 level mantle convection). Convergence rate 3 cm yr^{-1}. Figure conventions as in Fig. 7. (b) Experiments on simultaneous PLI and folding of 300 Ma old lithosphere with 'hot' mantle geotherm (=2 level mantle convection). Convergence rate 3 cm yr^{-1}. Figure conventions as in Fig. 7. (c) Experiments on simultaneous PLI and folding of 1000 Ma old lithosphere with 'hot' mantle geotherm (=2 level mantle convection). Convergence rate 3 cm yr^{-1}. Figure conventions as in Fig. 7. (d) Test experiment on simultaneous PLI and folding of 'reference' 150 Ma old lithosphere for 'cold' mantle geotherm (=whole mantle convection). Convergence rate 3 cm yr^{-1}. Figure conventions as in Fig. 7.

strongly amplify one of the fold anticlines; (3) in all cases of PLI and simultaneous folding, folding appears first to retard plume initialization but then it may deviate the trajectory of plume ascent towards one of the fold anticlines and (4) at early stages of its ascend, a plume may result in an increase of the mantle folding wavelength, at later stages plume-induced weakening is expected to lead to a decrease of the folding wavelength. The above conclusions depend naturally on the plume head size as the effect of PLI will be stronger for larger plume heads. We also tested several cases in which folding started 1 to 5 Myr before or after plume initialization. In these cases, upon arrival, the plume first increases the mantle-folding wavelength. Subsequently the folding wavelength is decreasing, favoring the development of an anticline situated above the centre of the plume head. When compression is exerted after

plume emplacement, folding develops with a reduced wavelength, basically above the plume head and potentially results in the inversion of plume-induced rift basins. However, full-scale exploration of the potential consequences of time lags between PLI and folding requires to cover time lags of up to 50–100 Myr and hence to conduct a very large number of additional experiments, which merits a separate study.

For all experiments we observed short timescales for topography creation and development of differential topography: a rapid temporal succession from ∼1000 m scale uplift at early stages of plume emplacement to only 100 m scale uplift at the same location during later stages and vice versa. In some of the latter cases the large-amplitude uplift is more localized as a mega anticline above the plume, whereas the low amplitude surface deflection is more
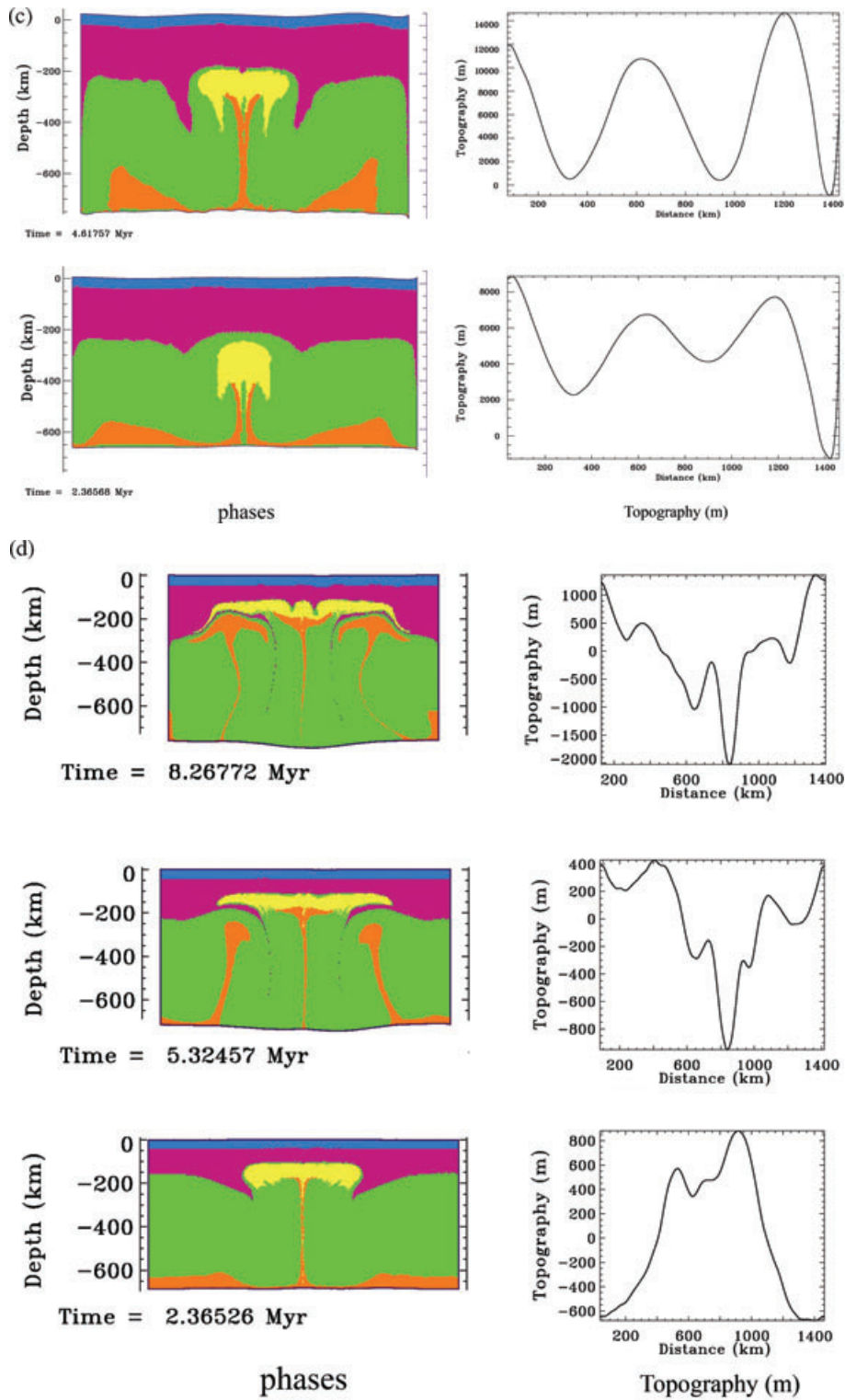
Figure 10. (*Continued.*)

periodically spread over a wide area. The age of the overlying litho-sphere appears to be a key factor for the temporal evolution of the development of the surface topography: The pattern of topography amplified in time observed for young lithosphere (60 Ma) is highly different from the patterns observed in case of PLI for the other ages (150, 300 and 1000 Ma)—with increasing age and strength of the lithosphere initial doming was short-lived and succeeded by

a series of spatially periodic subsidence-uplift patterns. Although down thrusting of mantle and plume material is clearly observed in the presence of compression, it is also well expressed in the experiments without compression (see Section 5.1). However, it appears that down thrusting is somewhat magnified by compression. We also note the differences in the style of mantle down thrust-ing: thick-skinned down thrusting in case of 60-Ma-old lithosphere

versus thin-skinned down thrusting in case of older lithospheres. This observation is, however, also valid for the cases without convergence.

6 DISCUSSION AND CONCLUSIONS

The major differences between the effect of tectonically induced folding and plume impingement on the lithosphere refer to (1) omni-directional, in case of homogeneous lithosphere, character of deformation produced by a plume compared to directional deformation produced by folding; (2) folding produces significantly larger vertical amplitudes; (3) the response of the lithosphere to folding is quasi-instantaneous, yet, depending on the rate of shortening, significant amplitudes of folding take time (of the order of a few Myr) to develop; on the other hand, there is a certain time lag (about 0.5 Myr) between the time of plume initialization at depth and reaction of the surface to this initialization, yet the growth rate of topography in this case is rapid; (4) timescales of folding and PLI-related deformation (considering upper mantle plumes only) are on the order of few millions to at most a few tens of millions of years, and tend to be longer in case of stronger lithospheres; (5) folding-induced vertical motions result in progressive amplification of initial synclines and anticlines (basins become deeper, uplifts grow), whereas PLI induced deformation significantly varies in time, for example, zones of surface depression may be replaced by zones of surface uplift and vice versa and (6) folding requires a considerable competence contrast between the lithosphere and underlying asthenosphere, that is, it does not develop in young continental plates.

6.1 Model diagnostics for plumes

Our experiments adopt realistic plate formulations and suggest that plumes can largely affect lithospheric evolution (e.g. plate break-off, extension and compression, mantle and crustal down-warping). They also show that surface expressions of PLI may be quite complex (i.e. quite different from the long-wavelength dynamic topography derived from conventional models). In particular, a plume may produce periodic zones of surface compression and extension associated with small and intermediate wavelengths of deformation ($\lambda = 50, 200, 300, \ldots, 600$ km) that are more commonly associated with tectonic processes.

The plume impact is most significant in case of a young lithosphere (age <150 Ma) where it produces a series of basins and compressional zones with wavelengths as small as $\lambda = 50$ km and quite large (several thousand m) vertical amplitudes. Plume impact results in removal of mantle lithosphere that is down-warped to a great depth. Crust is extended and rifted above the plume head but compressional zones are also formed above the edges of the spreading plume head. As plume material flattens horizontally, it underlies the lithosphere over large distances that exceed by a factor of 5 the initial diameter of the plume, even in cases when the plume tail is disconnected from the source region. The geodynamic influence of this material can be felt during 50–100 Myr after the plume emplacement. The predicted surface topography would be expected to possess a radial symmetry (in difference of that created by unidirectional tectonic deformation). However, the presence of inherited parallel structures within the lithosphere (e.g. series of cratonic blocks) may channelize plume head flow along their borders resulting in directional deformation.

The plume impact is significant also in case of older plates, specifically for the model representative for 300 Ma lithosphere.

In this case, the predicted surface wavelengths are larger and vertical amplitudes are smaller (up to 400–500 km and 1000–5000 m scale, respectively), but the overall effects are similar to the case of younger lithosphere; the plume erodes a major part of the lithospheric mantle resulting in a significant drop in the integrated strength of the lithosphere.

It appears that at passive margins, PLI may also result in gravitational disbalance leading to subduction of the continental lithosphere (e.g. Fig. 4).

PLI with strong non-depleted old lithosphere (age >300 Ma, dry olivine rheology) still produce very significant surface features, with wavelengths up to $\lambda = 600–800$ km and vertical uplifts in the order of several hundred meters. The bottom of the lithosphere is largely affected by plume-driven erosion and mantle down-warping that logically should result in melt infiltration from the plume to the mantle lithosphere.

In all cases, crust–mantle decoupling plays a very significant role for the lithospheric response during PLI. Strong decoupling results in a reduced effect of PLI at the surface and in the appearance of very small deformational wavelengths. In this case, a large part of the dynamic topography is compensated within the ductile crust.

The lithospheric response to a rising plume is characterized by some delay on the order of 0.1–0.5 Myr and can last for 10s to 100 Myr after the plume emplacement.

Finally, we conclude that even small-scale 'baby' plumes (note, however, that our study is limited to relatively small upper mantle plumes) may have significant impact on lithosphere evolution, in general for the plates younger than 300 Ma. Their effects are likely to be mitigated for older plates.

6.2 Model characteristics for folding

If the total amount of horizontal shortening exerted on a plate exceeds approximately 10 per cent, classical harmonic periodical instabilities, usually recognized as folding, may become highly aperiodic, or characterized by laterally varying wavelengths. In case of crust-mantle decoupling, folding is bi- or multiharmonic, with generally smaller crustal wavelengths ($\lambda < 100$ km) and a mantle wavelength on the order of $\lambda = 150–600$ km. Folding results in a drop of the integrated strength at the inflection points, and thus requires a smaller force to continue. However, with time, hot material advected below anticlines cools down, whereas down-folded cold parts of the plate get hotter. This results in re-arrangement of the integrated strength of the plate, so that it gets stronger in some (ductile) inflection points. The wavelength of deformation of a plate with horizontally variable strength is also variable horizontally. On the other hand, the initiated topography tends to be preserved with time, even after cessation of the forces that have provoked folding.

It should be noted that the amplitudes of folding predicted in the experiments with strong plates (e.g. experiment of Fig. 9a), even if very high, are mechanically consistent. In linear theory of folding, the amplitude of folding is not limited; it is some simple function of the amount of shortening. If the lithosphere is strong enough and the applied horizontal forces are sufficient to overcome its resistance and gravity forces, the lithosphere may fold to quite important amplitudes (except very thick plates in which pure shear deformation start to compete with folding). The results of the experiments, if properly scaled, are consistent with the previous models. For example, in case of the Fig. 9(a), the predicted amplitude of folding (40 km) is higher than in a similar numerical experiment made by Burg & Podladchikov (2000). However, this difference refers to a larger relative amount of shortening in our experiment:

500 km of shortening of an initially 1500-km-wide box in our model (Fig. 9a) compared to 500 km of shortening of an initially 2500 km wide box in the Burg & Podladchikov (2000) model. 25 km amplitude of folding obtained by Burg & Podladchikov (2000) scaled by 2500/1500 (=1.66) yields 41.6 km, that is, the maximal amplitude of folding that we have obtained in our model. However, at amounts of shortening >10 per cent, deviations from linear theory are important. Specifically the amplitude of folding is limited by $\rho g h$-to-plate strength ratio, 50-km-high folds imply normal stresses on the order of 1.5 GPa. This is the maximal differential strength of rocks in case of strongest rheologies predicted by rock mechanics (e.g. Burov 2007). In reality, rocks have smaller strengths (500–700 MPa) than predicted from laboratory experiments (Burov 2007). Consequently, real-world 'free air' folds would not have amplitudes larger than 15–20 km. However, if the syncline folds are timely filled with sediment, which basically not the case in nature (e.g. Cloetingh & Ziegler 2007), this would reduce the effect of gravity by up to 80 per cent allowing for very deep fold basins to be formed. On the other hand, surface processes maintain topography amplitudes at a certain level, and, as a result, very high anticline folds are uncommon (e.g. Guest *et al.* 2007). As shown in previous studies (e.g. Cloetingh *et al.* 1997), large amplitude folding finally leads to localization of deformation at one of the folds and the other folds die out after about 10 Myr of shortening.

It is also noteworthy that even though the maximal horizontal forces developed in the models with strong lithosphere (300 and 1000 Myr old plates) were smaller than 10^{13} N, this is still higher than the forces available from slab pull and ridge push (10^{12} N). Consequently, the maximal amplitudes of folding predicted in the experiments may be somewhat exaggerated. Note, however, that stresses can be amplified locally to higher levels due to plate geometry (e.g. Indo-Astralian Plate (Cloetingh & Wortel 1986).

6.3 Plume–folding interactions

Plume activity followed by folding may result in strong fold amplification in the area directly affected by a plume. However, if the plate has experienced a significant strength loss due to thermal re-activation by a plume, it will not fold at all due to insufficient competence contrasts between weak and strong layers.

Inversely, one would expect that folding activity followed by a thermal perturbation some time after onset of folding may be largely perturbed in terms of the wavelength, or even interrupted (significant strength loss). The anticlines of folds would serve to catch some of the hot plume material resulting in a specific spatial distribution of melting/volcanic activity.

6.4 Influence of phase changes and other parameters (discussion)

Until this point, the models presented in this study did not take into account the mineralogical phase changes that might be of importance for the development of mantle–lithosphere interactions. A number of authors have already questioned, within viscous models with no free surface, the relative importance of mineralogical phase changes and of the associated latent heating/cooling and partial melting for PLI (e.g. Christensen & Yuen 1985; Christensen 1995; Litasov & Ohtani 2007). Using a thermodynamically coupled phase change formulation (Appendix A2) that we have previously developed in Yamato *et al.* (2007, 2008), we have performed some additional test experiments using the thermodynamic petrology data

base and free energy minimization algorithm from Connolly (2005). This formulation allows to account for continuous density and elasticity changes in polyphase aggregates (five major mineralogical components of each rock are accounted for) as a function of *P–T* conditions. It also accounts for the associated latent heating/cooling (the viscous dissipation heating was switched off due to the uncertainties on heat conversion factors). This approach based on the assumption of state as function of *P–T* conditions might be not always sufficient because it is difficult to account for all possible states of a polyphase aggregate for given *P–T* conditions. However, it provides a better approximation for rock density than linearly changing coefficients of thermal expansion/compressibility or the approach based on bi-phase Claypeyron slopes traced for averaged specific heats that is mainly used in convection models (Schubert *et al.* 2001). This experiment refers to the 'reference' model setup with 300-Ma-old lithosphere and a 'hot' initial mantle geotherm (Figs 5a and b). As can be seen (Fig. 11), the main difference with the experiments of Figs 5a and b refers to the 'diffusive' behaviour of the plume tail and the absence of distinct density boundaries between plume and mantle (specifically between plume head and mantle). This may actually explain why 'baby-plumes' that have no pervasive deep sources can be hardly detectable from regional seismic tomography.

6.5 General conclusions

The results of our study suggest that plume activity may facilitate folding basically by lowering stresses needed for folding. Stress reduction may occur due to both thermal and structural weakening (crust mantle decoupling) and mechanical erosion of the plate by a plume. Yet, in case of a dramatic stress drop PLI may prohibit folding as the latter requires substantial stress/strength contrasts within the lithosphere. PLI may also prohibit folding at the initial stages of the plume impact as the associated flexural peripheral uprise provokes large-scale extension that works against the compression, that is, against folding. The impact of a plume also results in the reduction of the folding wavelength (by weakening of the plate) and localization of folding above the plume impact area. A general outcome of this study is that lithospheric folding as a mechanism for producing thermal perturbations in the lithosphere/upper mantle system appears to be a less feasible scenario than vice versa. The time lag between the plume impact and the onset of tectonic folding will also be crucial for the efficiency of the interaction between these processes.

As was found earlier, for slow convergence rates (<1.5 cm yr^{-1}) no folding in young lithosphere (age <150 Ma) can be induced by far-field forces. This point is Important in connection with atypical folding in some recently formed sedimentary basins such as the Pannonian Basin, and may serve for discrimination between expected plume and folding impact on young lithospheres.

Slow convergence promotes lithospheric mantle (and sometimes crustal) down thrusting above plume borders and horizontal spreading of plume heads. Fast convergence enhances folding in cratonic lithospheres.

It might be important to note for the ongoing discussion on the Eifel/Massif Central plumes (Ritter *et al.* 2001) that folding inside Europe is limited to the position of Palaeozoic massifs, including also the Armorican massif (Cloetingh & Van Wees 2005)

Plume-induced thermomechanical erosion of the bottom of young (age 150 Ma) and intermediate age lithospheres (age <300–700 Ma) appears to be a very important mechanism that may result
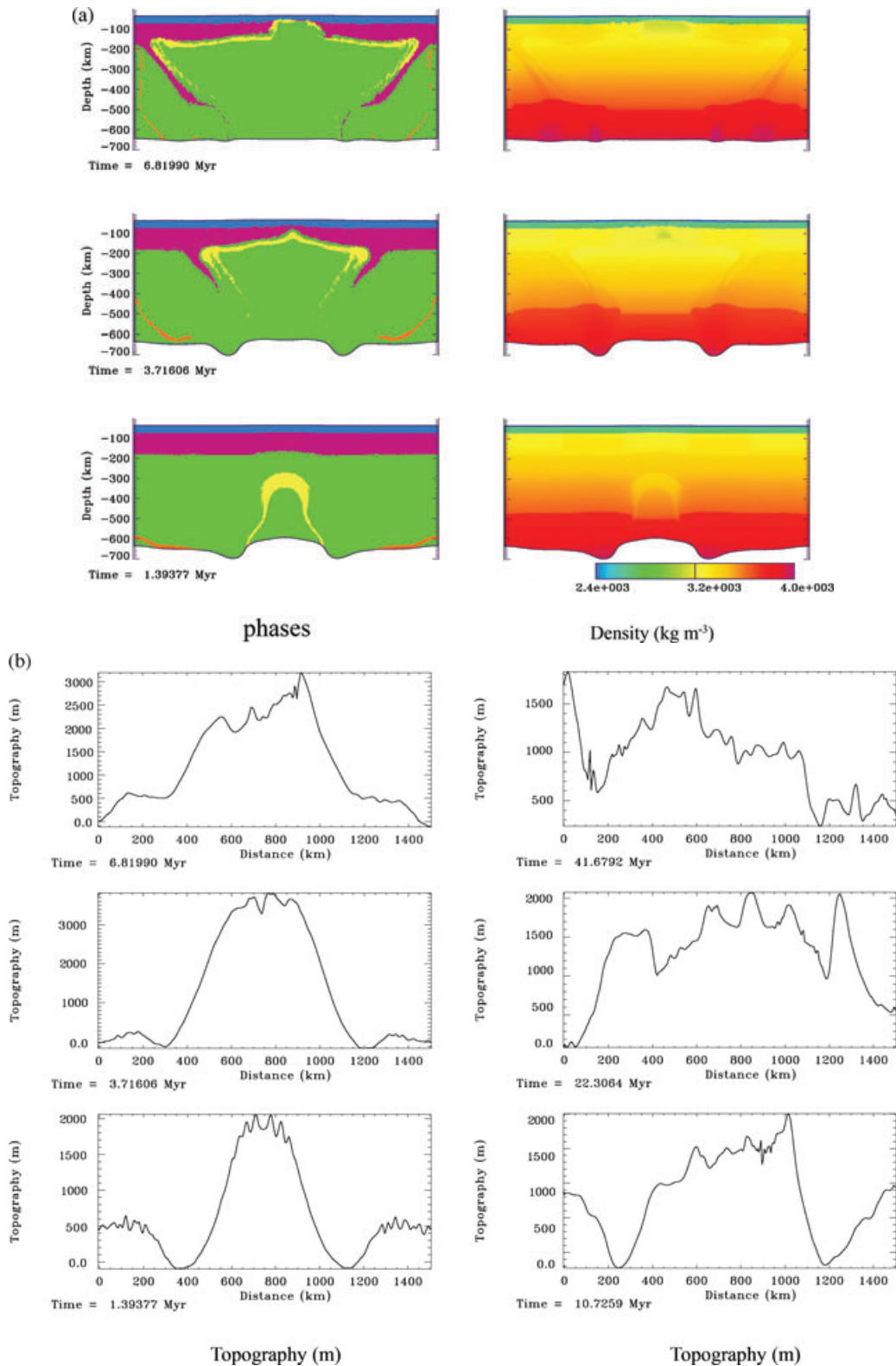
Figure 11. (a) Test experiment similar to that of Figs 5(a) and (b) but with full account for thermodynamic phase changes for mineralogical phases used in the reference experiment (300 Ma lithosphere and 'hot' mantle geotherm, Figs 5a and b). Left-hand panel: material phases. Right-hand panel: dynamically updated density distribution (Appendix A2). As can be seen, the main difference with the results of the reference experiment refers to the 'diffusive' behaviour of the plume tail and the absence of distinct density boundaries between plume and mantle (specifically between the plume head and mantle), which probably explains why 'baby-plumes' that have no pervasive deep sources are hardly detectable from regional seismic tomography. (b) Surface topography evolution for the experiment shown in (a) (left-hand panel, 1.3–6.8 Myr) and long-term topography evolution after plume head emplacement (right-hand panel, 10–41 Myr).

in thinning (by a factor of 2 or more) and rejuvenation of the lithosphere above the plume head over very large distances (1000 km), resulting in formation of thin lithospheric blocks surrounded by thicker lithosphere, with deep mantle and crustal down-warping (or delamination) at the borders with the thinned areas. In compressional settings, such thinning will favour onset of large-scale folding with variable wavelengths.

6.6 Some remaining questions

It appears that high rate shortening may prevent the development of distinct plume heads below the lithosphere. This might be an explanation for observed baby plumes without plume heads in the intraplate lithosphere domains of Europe (Ritter *et al.* 2001), which are currently under compression.

It is likely that in case of PLI the characteristic wavelengths of folding may not conform the theoretical relations between thermomechanical age and wavelength observed for folding.

Furthers development is needed to fully account for thermodynamic phase changes associated with PLI. In particular, *P–T* based approach might be insufficient as it does not allow to fully trace all possible states of polyphase aggregates. This will allow to compute consistent synthetic seismic velocity anomalies (with account for composition, inelasticity and anharmonicity) and directly compare them with the data of seismic tomography.

REFERENCES

Allen, M.B. & Davies, C.E., 2007. Unstable Asia: active deformation of Siberia revealed by drainage shifts, *Basin Res.,* **19,** 379–392.

Argus, D.F., Peltier, W.R. & Watkins, M.M., 1999. Glacial isostatic adjustment observed using very long baseline interferometry and satellite laser ranging geodesy, *J. geophys. Res.,* **104**(B12), 29 077–29 093.

Arrowsmith, S.J., Kendall, M., White, N., VanDecar, J.C. & Booth, D.C., 2005. Seismic imaging of a hot upwelling beneath the British Isles, *Geology,* **33,** 345–348.

Artemieva, I.M., Thybo, H. & Kaban, M.K., 2006. Deep Europe today: Geophysical synthesis of the upper mantle structure and lithospheric processes over 3,5 Ga, in *European Lithosphere Dynamics,* pp. 11–42, eds Gee, D. & Stephenson, R., Geol. Soc. London Memoirs 32.

Avouac, J.-P. & Burov, E.B., 1996. Erosion as a driving mechanism of intracontinental mountain growth, *J. geophys. Res.,* **110,** 17 747–17769.

Babault, J., Teixelll, A., Arboleya, M.L. & Charroud, M., 2008. A Late Cenozoic age for long-wavelength surface uplift of the Atlas Mountains of Morocco, *Terra Nova,* **20,** 102–107.

Bada, G., Cloetingh, S., Gerner, P. & Horváth, F., 1998. Sources of recent tectonic stress in the Pannonian region: inferences from finite element modelling, *Geophys. J. Int.,* **134,** 87–101.

Bada, G. *et al.*, 2007. Motion of Adria and ongoing inversion of the Pannonian basin: seismicity, GPS velocities and stress transfer, in *Continental Intraplate Earthquakes: Science, Hazard, and Policy Issues,* pp. 243–262, eds Stein, S. & Mazzotti, S., GSA Special Paper 425.

Barth, A., Jordan, M. & Ritter, J.R.R., 2007. Crustal and upper mantle structure of the French Massif Central plume, in *Mantle Plumes—A Mul-*

tidisciplinary Approach, pp. 159–184, eds Ritter, J.R.R. & Christensen, U.R., Springer Verlag, Heidelberg.

Batchelor, G.K., 1967. *An Introduction to Fluid Dynamics,* Cambridge Univ. Press, Cambridge, UK, 662 pp.

Bellahsen, N., Daniel, J.-M., Bollinger, L. & Burov, E., 2003. Influence of ductile layers on growth of normal faults: insights from analogue and numerical models, *J. Struct. Geol.,* **25,** 1471–1485.

Bercovici, D., Ricard, Y. & Schubert, G., 2001. A two-phase model for compaction and damage 3. Applications to shear localization and plate boundary formation, *J. geophys. Res.,* **106,** 8925–8939.

Bijwaard, H. & Spakman, W., 1999. Tomographic evidence for a narrow whole mantle plume below Iceland, *Earth. planet. Sci. Lett.,* **166,** 121–126.

Bijwaard, H. & Spakman, W., 2000. Non-linear global P-wave tomography by iterated linearized inversion, *Geophys. J. Int.,* **141,** 71–82.

Biot, M.A., 1961. Theory of Folding of Stratified viscoelastic media and its implications in tectonics and orogenesis, *Geol. Soc. Am. Bull.,* **72,** 1595–1620.

Bott, M.H.P. & Bott, J.D.J., 2004. The Cenozoic uplift and earthquake belt of mainland Britain as a response to an underlying hot, low-density mantle, *J. Geol. Soc.,* **161,** 19–29.

Bourgeois, O., Ford, M., Diraison, M., Le Carlier de Veslud, C., Gerbault, M., Pik, R., Nuby, N. & Bonnet, S., 2007. Separation of rifting and lithospheric folding signatures in the NW-Alpine foreland, *Int. J. Earth Sci.,* **96,** 1003–1031.

Burg, J.-P. & Podladchikov, Y., 2000. From buckling to asymmetric folding of the continental lithosphere: numerical modelling and application to the Himalayan syntaxes, in *Tectonics of the Nanga Parbat Syntexis and the Western Himalaya and Karakoram,* Spec. Pub. 170, pp. 219–236, eds Asif Khan, M., Qasim Jan, M., Treloar, P.J. & Searle, M.P., Geol. Soc. London.

Burov, E.B., 2007. Plate rheology and mechanics, in *Treatise on Geophysics,* Vol. 6: Crust and Lithosphere Dynamics, pp. 99–152, ed. Schubert, G., Elsevier, Amsterdam, ISBN:978-0-444–51928-3.

Burov, E.B. & Cloetingh, S., 1997. Erosion and rift dynamics: new thermalmechanical aspects of post-rift evolution of extensional basins, *Earth. planet. Sc. Lett.,* **150,** 7–26.

Burov, E.B. & Diament, M., 1995. Effective Elastic Thickness of the continental lithosphere—what does it really mean?, *J. geophys. Res.,* **100,** 3905–3927.

Burov, E. & Diament, M., 1996. The effective elastic thickness (EET) and inelastic rheology of continents and oceans, *Geology,* **24,** 419–423.

Burov, E.B. & Guillou-Frottier, L., 2005. The plume head–continental lithosphere interaction using a tectonically realistic formulation for the lithosphere, *Geophys. J. Int.,* **161,** 469–490.

Burov, E. & Molnar, P., 1998. Gravity anomalies over the Ferghana Valley (central Asia), and intracontinental deformation, *J. geophys. Res.,* **103,** 18 137–18 152.

Burov, E. & Poliakov, A., 2001. Erosion and rheology controls on syn- and post-rift evolution: verifying old and new ideas using a fully coupled numerical model, *J. geophys. Res.,* **106,** 16 461–16 481.

Burov, E. & Watts, A.B., 2006. The long-term strength of continental lithosphere: "jelly-sandwich" or "crème-brûlé"? *GSA Today,* **16**(1), pp. 4–10, doi:10.1130/1052-5173(2006)016<4:TLTSOC>2.0.CO;2.

Burov, E., Lobkovsky, L., Cloetingh, S. & Nikishin, A., 1993. Continental lithosphere folding in Central Asia. Part 2: constraints from gravity and topography, *Tectonophysics,* **226,** 73–87.

Burov, E.B., Jolivet, L., Le Pourhiet, L. & Poliakov, A., 2001. A thermomechanical model of exhumation of HP and UHP methamorphic rocks in Alpine mountain belts, *Tectonophysics,* **342,** 113–136.

Burov, E., Jaupart, C. & Guillou-Frottier, L., 2003. Emplacement of magma reservoirs in the upper crust, *J. geophys. Res.,* **108** (B4), 2177, doi:10.1029/2002JB001904.

Burov, E., Guillou-Frottier, L., d'Acremont, E., Le Pourhiet, L. & Cloetingh, S., 2007. Plume head–lithosphere interactions near intra-continental plate boundaries, *Tectonophysics,* **434,** 15–38.

Byerlee, J.D. & Friction of rocks, 1978. *Pure appl. Geophys.,* **116,** 615–626.

Carter, N.L. & Tsenn, M.C., 1987. Flow properties of continental lithosphere, *Tectonophysics,* **36,** 27–63.

Castellanos, D., De Vicente, G. & Vegas, R., 2002. Lithospheric folding in Iberia, *Tectonics,* **21,** 1041, doi:10.1029/2001TC901031.

Cavazza, W., Roure, F., Spakman, W., Stampfli, G.M. & Ziegler, P.A. (eds), 2004. *The TRANSMED Atlas. The Mediterranean Region from Crust to Mantle: Geological and Geophysical Framework,* Publication of the Mediterranean Consortium for the 32nd International Geological Congress, XXIV, 141 pp.

Christensen, U.R., 1995. Effects of phase transitions on mantle convection, *Ann. Rev. Earth planet. Sci.,* **23,** 65–87.

Christensen, U. & Yuen, D.A., 1985. Layered convection induced by phase transitions, *J. geophys. Res.,* **90,** 10 291–10 300.

Clauser, C., 2006. Geothermal Energy, in *Landolt-Börnstein Group VIII: Advanced Materials and Technologies,* Vol. 3: Energy Technologies, Subvol. C: Renewable Energies, pp. 493–604, ed. Heinloth, K., Springer Verlag, Heidelberg-Berlin.

Clift, P.D., 1999. The thermal impact of Palaeocene magmatic underplating in Faroe-Shetland-Rockall region, in *Petroleum Geology of Northwest Europe: Proceedings of the 5th Conference Geol.,* pp. 585–593, eds Fleet, A.J. & Boldy, S.A.R., Soc. London.

Cloetingh, S.A.P.L. & TOPO-EUROPE Working Group, 2007. TOPO-EUROPE: the geoscience of coupled deep Earth-surface processes, *Global. planet. Change,* **58,** 1–118.

Cloetingh, S. & van Wees, J.D., 2005. Strength reversal in Europe's intraplate lithosphere: transition from basin inversion to lithospheric folding, *Geology,* **33,** 285–288; doi:10.1130/G21051.1.

Cloetingh, S.A.P.L., Burov, E., Beekman, F., Andeweg, B., Andriessen, P.A.M. & Garcia Cloetingh and Wortel, 1986. Stress in the Indo-Australian plate, *Tectonophysics,* **132,** 49–67.

Cloetingh, S., Balen van, R.T., Voorde ter, M., Zoetemeijer, B.P. & Bezemer den, T., 1997. Mechanical aspects of sedimentary basin formation: development of integrated models for lithospheric and surface processes, *Geol. Rundsch.,* **86,** 226–240.

Cloetingh, S.A.P.L., Burov, E. & Poliakov, A., 1999. Lithosphere folding: Primary response to compression? (from central Asia to Paris basin), *Tectonics,* **18,** 1064–1083.

Cloetingh, S., Burov, E., Beekman, F., Andeweg, B., Andriessen, P.A.M., Garcia Castellanos, D., de Vicente, G. & Vegas, R., 2002. Lithospheric folding in Iberia, *Tectonics,* **21**(5), 1–26.

Cloetingh, S.A.P.L. *et al.* (TOPO-EUROPE Working Group), 2007. TOPO-EUROPE: the Geoscience of Coupled Deep Earth Surface Processes, *Global. planet. Change,* **58,** 1–118, doi:10.1016/J.gloplacha.2007.02.008.

Cloetingh, S.A.P.L. *et al.*, 2005. Lithospheric memory, state of stress and rheology: neotectonic controls on Europe's intraplate continental topography, *Quater. Sci. Rev.,* **24,** 241–304.

Cloetingh, S., Cornu, T., Ziegler, P.A., Beekman, F. & ENTEC Working Group, 2006. Neotectonics and intraplate continental topography of the northern Alpine Foreland, *Earth. Sci. Rev.,* **74,** 127–196.

Condie, K.C., Des Marais, D.J. & Abbott, D., 2000. Geologic evidence for a mantle superplume event at 1.9 Ga, *Geochem. Geophys. Geosyst.,* **1**(12), doi:10.1029/2000GC000095.

Connolly, J.A.D., 2005. Computation of phase equilibria by linear programming: a tool for geodynamic modeling and its application to subduction zone decarbonation, *Earth planet. Sci. Lett.,* **236,** 524–541.

Corchete, V., Chourak, M., Khattach, D. & Benaïm, E.H., 2007. The high-resolution gravimetric geoid of Morocco, *J. Afric. Earth Sci.,* **48,** 267–272.

Courtillot, V., Davaille, A., Besse, J. & Stock, J., 2003. Three distinct types of hotspots in the Earth's mantle, *Earth planet. Sci. Lett.,* **205,** 295–308.

Cserepes, L., Christensen, U.R. & Ribe, N.M., 2000. Geoid height versus topography for a plume model of the Hawaiian swell, *Earth planet. Sci. Lett.,* **178,** 29–38.

Cundall, P.A., 1989. Numerical experiments on localization in frictional materials, *Ing. Arch.,* **59,** 148–159.

d'Acremont, E., Leroy, S. & Burov, E.B., 2003. Numerical modelling of a mantle plume: the plume head-lithosphere interaction in the formation of an oceanic large igneous province, *Earth planet. Sci. Lett.,* **206,** 379–396.

Davies, G.F., 1994. Thermomechanical erosion of the lithosphere by mantle plumes. *J. geophys. Res.,* **99,** 15 709–15 722.

De Vicente, G. *et al.*, 2007. Cenozoic thick-skinned deformation and topography evolution of the Spanish Central System, *Global. planet. Change,* **58,** 335–381.

De Vicente, G., Cloetingh, S., Muñoz-Martín, A., Olaiz, A., Stich, D., Vegas, R., Galindo-Zaldívar, J. & Fernández-Lozano, J., 2008. Inversion of moment tensor focal mechanisms for active stresses around the Microcontinent Iberia: tectonic implications, *Tectonics,* **27,** TC1009, doi:10.1029/2006TC002093.

Dèzes, P., Schmid, S.M. & Ziegler, P.M., 2004. Evolution of the European Cenozoic Rift System: interaction of the Alpine and Pyrenean orogens with their foreland lithosphere, *Tectonophysics,* **389,** 1–33.

Doin, M.-P., Fleitout, L. & Christensen, U., 1997. Mantle convection and stability of depleted and undepleted continental lithosphere, *J. geophys. Res.,* **102,** 2771–2787.

Dombrádi, E., Sokoutis, D., Bada, G., Cloetingh, S. & Horváth, F., 2008. Large-scale lithospheric folding controlling active deformation and topography development in the Pannonian basin: insights from analogue modelling, in *Geophysical Research Abstracts,* Vol. 10, EGU General Assembly 2008, EGU2008-A-08002.

Doré, A.G., Scotchmana, I.C. & Corcoran, D., 2000. Cenozoic exhumation and prediction of the hydrocarbon system on the NW European margin. *J. Geochem. Explor,* **69–70,** 615–618.

Faleide, J.I., Tsikalas, F., Breivik, A.J., Mjelde, R., Ritzmann, O., Engen, Ø., Wilson, J. & Eldholm, O., 2008. Structure and evolution of the continental margin off Norway and the Barents Sea, *Episodes,* **31**(1), 82–91.

Farnetani, C.G. & Richards, M.A., 1994. Numerical investigations of the mantle plume initiation model for flood basalt events, *J. geophys. Res.,* **99,** 13 813–13 833.

Fernández-Lozano, Sokoutis, D., Willingshofer, E., Cloetingh, S. & De Vicente, G., 2008. Lithospheric-scale folding in Iberia: Insights from analogue models, in *Geophysical Research Abstracts,* Vol. 10, EGU General Assembly 2008, EGU2008-A-09243.

Foulger, G.R. *et al.*, 2000. The seismic anomaly beneath Iceland extends down to the mantle transition zone and no deeper, *Geophys. J. Int.,* **142,** F1–F5.

Gemmer, L. & Houseman, G.A., 2007. Convergence and extension driven by lithospheric gravitational instability: evolution of the Alpine–Carpathian–Pannonian system, *Geophys. J. Int.,* **168,** 1276–1290, doi:10.1111/j.1365-246X.2006.03327.x.

Gerbault, M., Poliakov, A.N.B. & Daignières, M., 1998. Prediction of faulting from the theories of elasticity and plasticity; what are the limits? *J. Struct. Geol.,* **20,** 301–320.

Gerbault, M., Burov, E., Poliakov, A. & Dagnieres, M., 1999. Do faults trigger folding in the asthenosphere? *Geophys. Res. Lett.,* **26**(2), 271–274.

Ghorbal, B., Bertotti, G., Foeken, J. & Andriessen, P., 2008. Unexpected Jurassic to Neogene vertical movements in "stable" parts of NW Africa revealed by low temperature geochronology, *Terra Nova,* **20/5,** 363–553.

Goetze, C. & Evans, B., 1979. Stress and temperature in bending lithosphere as constrained by experimental rock mechanics, *Geophys. J. R. astr. Soc.,* **59,** 463–478.

Goes, S., Spakman, W. & Bijwaard, H., 1999. A lower mantle source for central European volcanism, *Science,* **286,** 1928–1931.

Goes, S., Govers, R. & Vacher, P., 2000. Shallow mantle temperatures under Europe from P and S wave tomography, *J. geophys. Res.,* **105**(11), 153–169.

Gölke, M. & Coblentz, D.D., 1996. Origin of the European regional stress field, *Tectonophysics,* **266,** 11–24.

Granet, M., Wilson, M. & Achauer, U., 1995. Imaging mantle plumes beneath the French Massif Central, *Earth. planet. Sci. Lett.,* **136,** 199–203.

Grenerczy, G., Sella, G.F., Stein, S. & Kenyeres, A., 2005. Tectonic implications of the GPS velocity field in the northern Adriatic region, *Geophys. Res. Lett.,* **32,** L16311.

Guest, B., Guest, A. & G. Axen, 2007. Late Tertiary tectonic evolution of northern Iran: a case for simple crustal folding, *Global planet. Change,* **58,** 435–453.

Guillou-Frottier, L., Burov, E., Nehlig, P. & Wyns, R., 2007. Deciphering plume-lithosphere interactions beneath Europe with topographic signatures, *Global planet. Change,* **58,** 119–140.

Herzberg, C., 1995. Generation of plume magmas through time: an experimental perspective, *Chem. Geol.,* **126,** 1–16.

Hoernle, K., Zang, Y.-S. & Graham, D., 1995. Seismic and geochemical evidence for large-scale mantle upwelling beneath the eastern Atlantic and Western and Central Europe, *Nature,* **374,** 34–39.

Horvath, F., Bada, G., Szafián, P., Tari, G., Adám, A. & Cloetingh, S., 2006. Formation and deformation of the Pannonian basin: constraints from observational data, *Geol. Soc. London, Memoirs,* **32,** 207–221.

Horváth, F. & Cloetingh, S., 1996. Stress-induced late-stage subsidence anomalies in the Pannonian basin, *Tectonophysics,* **266,** 287–300.

Hunt, G., Muhlhaus, H., Hobbs, B. & A. Ord, 1996. Localized folding of viscoelastic layers, *Geol. Rundsh.,* **85,** 58–64.

Japsen, P. & Chalmers, J.A., 2000. Neogene uplift and tectonics around the North Atlantic: overview, *Global Planet. Change,* **24,** 165–173.

Jarosiński, M., Beekman, F., Bada, G. & Cloetingh, S., 2007. Redistribution of recent collision push and ridge push in Central Europe: insights from FEM modelling, *Geophys. J. Int.,* **167,** 860–880.

Jaupart, C., Labrosse, S. & Mareschal, J.-C., 2007. Temperature, Heat and Energy in the Mantle of the Earth, in *Treatise on Geophysics*, Vol. 7: Mantle Dynamics, pp. 253–303, ed. Bercovici, D., Elsevier, Boston.

Jellinek, A.M., Gonnermann, H.M. & Richards, M.A., 2003. Plume capture by divergent plate motions: implications for the distribution of hotspots, geochemistry of mid-ocean ridge basalts, and estimates of the heat flux at the core-mantle boundary, *Earth planet. Sci. Lett.,* **205,** 361–378.

Kirby, S.H. & Kronenberg, A.K., 1987. Rheology of the lithosphere: selected topics, *Rev. Geophys.,* **25,** 1219–1244.

Kohlstedt, D.L., Evans, B. & Mackwell, S.J., 1995. Strength of the lithosphere: constraints imposed by laboratory experiments, *J. geophys. Res.,* **100,** 17 587–17 602.

Koulakov, I., Kaban, M.K., Tesauro, M. & Cloetingh, S., 2009. P and S velocity anomalies in the upper mantle beneath Europe from tomographic inversion of ISC data, *Geophys. J. Int.,* in press, doi:10.1111/j.1365-246X.2009.04279.x.

Lefort, J.P. & Agarwal, B.N.P., 1996. Gravity evidence for an Alpine buckling of the crust beneath the Paris Basin, *Tectonophysics,* **258,** 1–14.

Litasov, K.D. & Ohtani, E., 2007. Effect of water on the phase relations in Earth's mantle and deep water cycle, in *Advances in High-Pressure Mineralogy,* pp. 115–146, ed. Ohtani, E., Geol. Soc. Am. Spec. Paper 421.

Lithgow-Bertelloni, C. & Gurnis, M., 1997. Cenozoic subsidence and uplift of continents from time-varying dynamic topography, *Geology,* **25,** 735–738.

Lundin, E. & Dore, A.G., 2002. Mid-Cenozoic post-breakup deformation in the 'passive' margins bordering the Norwegian-Greenland Sea, *Mar. Petrol. Geol.,* **9,** 79–93.

Lustrino, M. & Carminati, E., 2007. Phantom plumes in Europe and the circum-Mediterranean region, *Geol. Soc. Amer. Spec. Publ.,* **430,** 723–745.

McKenzie, D., 1978. Some remarks on the development of sedimentary basins, *Earth planet. Sci. Lett.,* **40,** 25–32.

Meissner, R., 1986. The continental crust—a geophysical approach, in *International Geophysics Series,* Vol. 34, pp. 394–414, Academic Press, Orlando.

Missenard, Y., Zeyen, H., Frizon de Lamotte, D., Leturmy, P., Petit, C., Sébrier, M. & Saddiqi, O, 2006. Crustal versus asthenospheric origin of relief of the Atlas Mountains of Morocco, *J. geophys. Res.,* **111,** B03401, doi:10.1029/2005JB003708.

Mitrovica, J.X., Beamont, C. & Jarvis, G.T., 1989. Tilting of continental interiors by the dynamical effects of subduction, *Tectonics,* **8,** 1079–1094.

Montelli, R., Nolet, G., Dahlen, F.A., Masters, G., Engdahl, E.R. & Hung, S.H., 2004. Finite-frequency tomography reveals a variety of plume in the mantle, *Science,* **303,** 338–343.

Nyblade, A.A. & Sleep, N.H., 2003. Long lasting epeirogenic uplift from mantle plumes and the origin of the Southern African Plateau, *Geochem, Geophys. Geosyst.,* **4** (2003GC000573)

Parsons, B. & Sclater, J.G., 1977. An analysis of the variation of ocean floor bathymetry and heat flow with age, *J. geophys. Res.,* **82,** 803–827.

Pérez-Gussinyé, M. & Watts, A.B., 2005. The long-term strength of Europe and its implications for plate forming processes, *Nature,* **436,** 381–384.

Pilidou, S., Priestley, K., Debayle, E. & Gudmundsson, O., 2005. Rayleigh wave tomography in the North Atlantic: high resolution images of the Iceland, Azores and Eifel mantle plumes, *Lithos,* **79,** 453–474.

Piromallo, C. & Morelli, A., 2003. P wave tomography of the mantle under the Alpine Mediterranean area, *J. geophys. Res.,* **108,** 2065.

Poliakov, A.N.B., Cundall, P., Podladchilov, Y. & Laykhovsky, V., 1993. An explicit inertial method for the simulation of visco-elastic flow: an evaluation of elastic effects on diapiric flow in two- or three-layers models, in *Flow and Creep in the Solar System: Observations, Modelling and Theory, Dynamic Modelling and Flow in the Earth and Planet Series*, pp. 175–195, eds Stone, D.B. & Runcorn, S.K., Kluwer Academic, Dordrecht.

Ramberg, H., 1961. Contact strain and folding instability of multilayered body under compression, *Geol. Rundsch.,* **51,** 405–439.

Ranalli, G., 1995. *Rheology of the Earth,* 2nd edn, Chapman and Hall, London, 413 pp.

Ribe, N.M. & Christensen, U.R., 1994. Three-dimensional modeling of plume-lithosphere interaction, *J. geophys. Res.,* **99,** 669–682.

Ritter, J.R.R., 2005. Small-scale mantle plumes: imaging and geodynamic aspects, in perspectives in modern geology, in *Lectures Notes in Earth Sci.,* Vol. 105, pp. 69–94, ed. Wenzel, F., Springer Verlag, Heidelberg.

Ritter, J.R.R., Jordan, M., Christensen, U.R., Achauer, U., 2001. A mantle plume below the Eifel volcanic fields, Germany, *Earth. planet. Sci. Lett.,* **186,** 7–14.

Ritzmann, O. & Faleide, J.I., 2009. The crust and mantle lithosphere in the Barents Sea/Kara Sea region, *Tectonophysics,* **470,** 89–104.

Robin C., Allemand, P., Burov, E., Doin, M.P., Guillocheau, F., Dromart, G. & Garcia, J.P., 2003. Thermo-mechanical characteristics of the Paris Basin (Triassic-Pleistocene): from 3D stratigraphic database to numerical models. in *New Insights into Structural Interpretation and Modeling,* pp. 225–250, ed. Nieuwland, D.A., Geol. Soc. , London, Spec. Publ. 212.

Rohrmann, M., Van Der Beek, P.A., Van Der Hilst, R.D. & Reemst, P., 2002. Timing and mechanisms of North Atlantic Cenozoic uplift: evidence for mantle dwelling, in *Exhumation of the North Atlantic Margin: Timing, Mechanisms and Implications for Petroleum Exploration,* pp. 27–45, eds Dore, A.G., Cartwright, J.A., Stoker, M.S., Turner, J.P. & White, N., Geol. Soc., London, Spec. Publ. 196.

Romanowicz, B. & Gung, Y.C., 2002. Superplumes from the core-mantle boundary to the base of the lithosphere, *Science,* **296,** 513–516.

Scheck-Wenderoth, M. & Maystrenko, Y., 2008. How warm are passive continental margins? A 3D lithosphere-scale study from the Norwegian margin, *Geology,* **36,** 419–422.

Schmeling, H. & Marquart, G., 1990. A mechanism for crustal thinning without lateral extension, *Geophys. Res. Lett.,* **17,** 2417–2420.

Schmeling, H. & Marquart, G., 1993. Mantle flow and the evolution of the lithosphere, *Phys. Earth planet. Int.,* **79,** 241–267.

Schubert, G., Turcotte, D.L. & Olson, P., 2001. *Mantle Convection in the Earth and Planets,* Cambridge University Press, Cambridge, UK.

Skogseid, J., Planke, S., Faleide, J.L, Pedersen, T., Eldholm, O. & Neverdal, F., 2000. NE Atlantic continental rifting and volcanic margin formation, in *Dynamics of the Nonvegian Margin,* pp. 295–326, ed. Nottvedt, A., Geol. Soc. London, Spec. Publ. 167.

Sleep, N.H., 1997. Lateral flow and ponding of starting plume material, *J. geophys. Res.,* **102,** 10 001–10 012.

Sleep, N.H.H, 2003a. Fate of mantle plume material trapped within a lithospheric catchment with reference to Brazil, *Geochem. Geophys. Geosyst.,* **4,** 8509, doi:10.1029/2002GC000464.

Sleep, N., 2003b. Survival of Archean cratonal lithosphere, *J. geophys. Res.,* **108,** 2302, doi:10.1029/2001JB000169.

Sleep, N.H., 2003c. Geodynamic implications of xenolith geotherms, *Geochem. Geophys. Geosystems,* **4,** 1079, doi:10.1029/2003GC000511.

Sleep, N.H., 2006. Mantle plumes from top to bottom, *Earth Sci. Rev.,* **77,** 231–271.

Smelror, M. *et al.*, 2007. Towards a 4D topographic view of the Norwegian sea margin, *Global Planet. Change,* **58,** 382–410.

Smith, R.B., 1979. The folding of a strongly non-Newtonian layer, *Am. J. Sci.,* **279,** 272–287.

Sobolev, S.V. & Babeyko, A.Yu., 1994. Modeling of mineralogical composition, density and elastic wave velocities in anhydrous magmatic rocks, *Surv. Geophys.,* **15,** 515–544.

Sobolev, S.V., Zeyen, H., Granet, M., Achauer, U., Bauer, C., Werling, F., Altherr, R. & Fuchs, K., 1997. Upper mantle temperatures and lithosphere-asthenosphere system beneath the French Massif Central constrained by seismic, gravity, petrologic and thermal observations, *Tectonophysics,* **275,** 143–164.

Sokoutis, D., Burg, J.P., Bonini, M., Corti, G. & Cloetingh, S., 2005. Lithospheric-scale structures from the perspective of analogue continental collision, *Tectonophysics,* **406,** 1–15.

Solomatov, V.S., 1995. Scaling of temperature- and stress-dependent viscosity convection, Phys, *Fluids,* **7,** 266–274.

Solomatov, V.S. & Moresi, L.N., 2000. Scaling of time-dependent stagnant lid convection; application to small-scale convection on Earth and other terrestrial planets, *J. geophys. Res.,* **105,** 21795–21817.

Stephenson, R.A. & Lambeck, K., 1985. Isostatic response of the lithosphere with in-plane stress: application to Central Australia, *J. geophys Res.,* **90,** 8581–8588.

Tesauro, M., Hollenstein, C., Egli, R., Geiger, A. & Kahle, H.-G., 2005. Continuous GPS and broad-scale deformation across the Rhine Graben and the Alps, *Int. J. Earth. Sci.,* **94,** 525–537.

Tesauro, M., Kaban, M., Cloetingh, S., Hardebol, N. & Beekman, F., 2007. 3D strength and gravity anomalies of the European lithosphere, *Earth planet. Sci. Lett.,* **263,** 56–73.

Tesauro, M., Kaban, K. & Cloetingh, S., 2008. "EuCRUST-07: A new reference model for the European crust", *Geophys. Res. Lett.,* **35,** L05313, doi:10.1029/2007GL032244.

Thybo, H. & Anderson, D.L., 2006. The heterogeneous mantle, *Tectonophysics,* **416,** 1–6.

Trompert, R. & Hansen, U., 1998. Mantle convection simulations with rheologies that generate plate-like behaviour, *Nature,* **395,** 686–689.

Turcotte, D.L. & Schubert, G., 2002. *Geodynamics, Applications of Continuum Physics to Geological Problems,* 2nd edn, Cambridge Univ. Press, Cambridge.

Vagnes, E., Gabrielsen, R.H. & Haremo, P., 1998. Late Cretaceous – Cenozoic intraplate deformation at the Norwegian continental shelf: timing, magnitude and regional implications, *Tectonophysics,* **300,** 29–46.

van Keken, P., 1997. Evolution of starting mantle plumes: a comparison between numerical and laboratory models, *Earth planet. Sci. Lett.,* **148,** 1–11.

Weinberg, R.F. & Podladchikov, Y., 1994. Diapiric ascent of magmas through power law crust and mantle, *J. geophys. Res.,* **99,** 9543–9559.

White, N. & Lovell, B., 1997. Measuring the pulse of a plume with the sedimentary record, *Nature,* **387,** 888–891.

Wilson, M. & Bianchini, G., 1999. Tertiary-quaternary magmatism within the Mediterranean and surrounding regions, in *The Mediterranean Basins: Tertiary Extension within the Alpine Orogen,* pp. 141–168, eds Durand, B., Jolivet, L., Horvath, F. & Séranne, M., Geol. Soc., London, Spec. Publ. 156.

Wilson, M. & Patterson, R., 2001. Intraplate magmatism related to short-wavelength convective instabilities in the upper mantle: Evidence from the Tertiary-Quaternary volcanic province of Western and Central Europe, *Geol. Soc. Am. Spec. Publ.,* **352,** 37–58.

Wortel, M.J.R. & Spakman, W., 2000. Subduction and slab detachment in the Mediterranean-Carpathian region, *Science,* **290,** 1910–1917.

World Stress Map, 2007. World Stress Map, URL: http://www.world-stress-map.org/.

Wyns, F., Quesnel, F., Simon-Coïnçon, R., Guillocheau, F. & Lacquement, F., 2003. Major weathering in France related to lithospheric deformation, Paleoweathering and paleosurfaces in the Ardennes-Eifel region—Preizerdaul, Luxembourg, 14–17/mai/2003, *Géol. Fr.,* **1,** 79–97.

Yamato, P., Agard, P., Burov, E., Le Pourhiet, L., Jolivet, L. & Tiberi, C., 2007. Burial and exhumation in a subduction wedge: Mutual constraints from thermo-mechanical modelling and natural p-t-t data (sch. Lustres, w. Alps), *J. geophys. Res.,* **112,** B07410, doi:10.1029/2006JB004441.

Yamato, P., Burov, E., Agard, P., Le Pourhiet, L. & Jolivet, L., 2008. HP-UHP exhumation processes during continental subduction (W. Alps): when thermomechanical models reproduce P-T-t data, *Earth planet. Sci. Lett.,* **271,** 63–75.

Ziegler, P.A. & Dèzes, P., 2007. Neogene uplift of Variscan Massifs in the Alpine foreland: timing and controlling mechanisms, *Global. planet. Change.,* **58,** 237–269.

Ziegler, P.A., Van Wees, J.-D. & Cloetingh, S.A.P.L., 1998. Mechanical controls on collision.related compressional intraplate deformation, *Tectonophysics,* **300,** 103–129.

Zittelini, N., Cloetingh, S., D'Oriano, F. & Burov, E., 2009. Synclininal deformation as prime expression of intra-plate compressional deformation: the Atlantic segment of the Iberia-Africa Plate Boundary case study, *Geology,* submitted.

APPENDIX: NUMERICAL MODEL

A1 Basic equations

The Flamar-Para(o)voz is a FLAC-like code (Cundall 1989). It has a mixed finite-difference/finite element numerical scheme, with a Cartesian coordinate frame. We use a 2-D plane strain formulation. The Lagrangian mesh of Paravoz is composed of quadrilateral elements subdivided into two couples of triangular subelements with tri-linear shape functions. Para(o)voz is a large strain fully explicit time-marching algorithm. It locally solves full Newtonian equations of motion in a continuum mechanics approximation

$$\langle \rho \ddot{\mathbf{u}} \rangle - \nabla \boldsymbol{\sigma} - \rho \mathbf{g} = 0 \qquad (A1)$$

coupled with constitutive equations:

$$\frac{\mathrm{D}\sigma}{\mathrm{D}t} = F(\sigma, \mathbf{u}, \dot{\mathbf{u}}, \nabla\dot{\mathbf{u}}, ...T...) \qquad (A2)$$

and with equations of heat transfer (with heat advection term $\dot{\mathbf{u}}\nabla T$ included in the lagrangian derivative $\mathrm{D}T/\mathrm{D}t$)

$$\rho C_p \mathrm{D}T/\mathrm{D}t - k\nabla^2 T - \sum_{i}^{n} H_i = 0.$$

$$\rho = \rho_0[1 - \alpha(y)T + \beta(y)(-P)] \quad \text{or} \quad \rho = f(P, T). \qquad (A3a)$$

Here $\mathbf{u}, \boldsymbol{\sigma}, \mathbf{g}, k$ are the respective terms for displacement, stress, acceleration due to body forces and thermal conductivity. P is pressure (negative for compression). The triangular brackets in (A1) specify conditional use of the related term (in quasi-static mode inertial terms are damped using inertial mass scaling (Cundall 1989). The terms $t, \rho, \rho_0, C_p, T, H_i, \alpha(y), \beta(y)$ designate, respectively, time, density, density at reference conditions, specific heat, temperature, internal heat production, thermal expansion coefficient and isothermal compressibility. The symbol Σ means summation of various heats sources H_i. The expression $\rho = f(P, T)$, when used, refers to the formulation, in which phase changes are taken into account and density is computed by a thermodynamic module (Appendix A2) that evaluates the equilibrium density of constituent mineralogical phases for given P and T as well as latent heat contribution H_l to the term $\sum_{i}^{n} H_i$ ($\sum_{i}^{n} H_i = H_r + H_f + H_l + \cdots$). $\sum_{i}^{n} H_i$ also accounts for radiogenic heat H_r and frictional dissipation H_f. When the thermodynamic module is not used, H_l is set to zero and the value of $\alpha(y)$ varies as a simple linear function of depth, which roughly takes into account the fact that in the upper mantle $\alpha(y)$ drops by a factor of 2 at 650 km depth compared to its value at 100–250 km depth (Turcotte & Schubert 2002). Isothermal compressibility equals inverse bulk modulus (Tables 2 and 3); it was kept constant when

phase changes were not applied. The terms $D\sigma/Dt$, F are the objective Jaumann stress time derivative and a functional, respectively. In the Lagrangian method, incremental displacements are added to the grid coordinates allowing the mesh to move and deform with the material. This allows for the solution of large-strain problems while using locally the small-strain formulation: on each time step the solution is obtained in local coordinates, which are then updated in a large-strain mode.

Solution of (A1) provides velocities at mesh points used for computation of element strains and of heat advection $\mathbf{\dot{u}}\nabla T$. These strains are used in (A2) to calculate element stresses and equivalent forces used to compute velocities for the next time step. Due to the explicit approach, there are no convergence issues, which is rather common for implicit methods in case of non-linear rheologies. The algorithm automatically checks and adopts the internal time step using 0.1–0.5 of Courant's criterion of stability, which warrants stable solution.

A2 Explicit phase changes

Some test experiments (Fig. 11) have been completed using the direct solution for density, $\rho = f(P, T)$, obtained from direct optimization of Gibbs free energy for a typical mineralogical composition (five main mineralogical components) of the mantle, plume and lithosphere material. With that goal, the thermodynamic PERPLEX algorithm (Connolly 2005) has been coupled with the main code via (A3a) to introduce progressive density changes rather than using a fixed density grid based on metamorphic facies alone. PERPLEX minimizes free Gibbs energy G for a given chemical composition to calculate an equilibrium mineralogical assemblage for given P–T conditions

$$G = \sum_{i=1}^{n} \mu_i N_i, \tag{A3b}$$

where μ_i is the chemical potential and N_i the moles number for each component i constitutive of the assemblage. Given the mineralogical composition, the computation of density is straightforward (Yamato *et al.* 2007, 2008).

A3 Explicit elastic-viscous-plastic rheology

We use a serial (Maxwell type) body, in which the total strain increment in each numeric element is defined by a sum of elastic, viscous and brittle strain increments. Consequently, in contrast to fluid dynamic approaches, where non-viscous rheological terms are simulated using pseudo-plastic and pseudo-elastic viscous terms (e.g. Bercovici *et al.* 2001; Solomatov & Moresi 2000), our method explicitly treats all rheological terms. The parameters of elastic-ductile-plastic rheology laws for crust and mantle come from rock mechanics data (Tables 2 and 3; Kirby & Kronenberg 1987; Kohlstedt *et al.* 1995).

A3.1 Plastic (brittle) behaviour

The brittle behaviour of rocks is described by Byerlee's law (Byerlee 1978; Ranalli 1995), which corresponds to a Mohr–Coulomb material with friction angle $\phi = 30°$ and cohesion $|C_0| < 20$ MPa (e.g. Gerbault *et al.* 1998)

$$|\tau| = C_0 - \sigma_n \tan \phi, \tag{A4}$$

where σ_n is normal stress $\sigma_n = \frac{1}{3}\sigma_I + \sigma_{II}^{\text{dev}} \sin\phi$, $\frac{1}{3}\sigma_I = P$ is the effective pressure (negative for compression), σ_{II}^{dev} is the second invariant of deviatoric stress, or effective shear stress. The condition of the transition to brittle deformation (function of rupture f) reads as: $f = \sigma_{II}^{\text{dev}} + P \sin\phi - C_0 \cos\phi = 0$ and $\partial f/\partial t = 0$. In terms of principal stresses, the equivalent of the yield criterion (5) reads as

$$\sigma_1 - \sigma_3 = -\sin\phi(\sigma_1 + \sigma_3 - 2C_0/\tan\phi). \tag{A5}$$

A3.2 Elastic behaviour

The elastic behaviour is described by the linear Hooke's law

$$\sigma_{ij} = \lambda \varepsilon_{ii} \delta_{ij} + 2G\varepsilon_{ij}, \tag{A6}$$

where λ and G are Lame's constants. Repeating indexes mean summation and δ is the Kronecker's operator.

A3.3 Viscous (ductile) behaviour

Mantle convection and a part of lithospheric deformation are controlled by thermally activated creep (Kirby & Kronenberg 1987; Ranalli 1995). Within deep lithosphere and underlying mantle regions, creeping flow is non-Newtonian since the effective viscosity can vary within 10 orders of magnitude as a function of differential stress:

$$\dot{\varepsilon}^d = A(\sigma_1 - \sigma_3)^n \exp(-QR^{-1}T^{-1}), \tag{A7}$$

where $\dot{\varepsilon}^d$ is effective shear strain rate, A is a material constant, n is the power-law exponent, Q is the activation enthalpy, R is the universal gas constant, and T is temperature in K, σ_1 and σ_3 are the principal stresses. The effective viscosity μ_{eff} for this law is defined as

$$\mu_{\text{eff}} = \dot{\varepsilon}^{(1-n)/n} A^{-1/n} \exp[Q(nRT)^{-1}]. \tag{A8}$$

For non-uniaxial deformation, the law (A8) is converted to a triaxial form, using the invariant of strain rate and geometrical proportionality factors

$$\mu_{\text{eff}} = \dot{\varepsilon}_{II}^{d(1-n)/n}(A^*)^{-1/n} \exp[Q(nRT)^{-1}],$$

where

$$\dot{\varepsilon}_{II}^d = [Inv_{II}(\dot{\varepsilon}_{ij})]^{1/2} \quad \text{and} \quad A^* = 0.5A \cdot 3^{(n+1)/2} \tag{A9}$$

parameters A, n, Q are experimentally determined material constants (Tables 2 and 3). Using olivine parameters, one can verify that the predicted effective viscosity at the base of the lithosphere is 10^{19}–5×10^{19} Pa s matching post-glacial rebound data (Turcotte & Schubert 2002). In the depth interval of 250 km to 0 km the effective viscosity grows from 10^{19} to 10^{25}–10^{27} Pa s with decreasing temperature. Within the adiabatic temperature interval in the convective mantle, the dislocation flow law (A8) is replaced by a nearly Newtonian diffusion creep, which results in a quasi-constant mantle viscosity of 10^{19}–10^{21} Pa s (e.g. Turcotte & Schubert 2002). Weinberg & Podladchikov (1994) have also shown that the effective viscosity in close vicinity of an ascending diapir is influenced by the local strain rate field and partly by heat exchanges between the diapir and surrounding rock, which suggests possible localized phase changes.